IntechOpen

Medical Imaging and Image-Guided Interventions

Edited by Ronnie A. Sebro

MEDICAL IMAGING AND IMAGE-GUIDED INTERVENTIONS

Edited by **Ronnie A. Sebro**

Medical Imaging and Image-Guided Interventions
http://dx.doi.org/10.5772/intechopen.70299
Edited by Ronnie A. Sebro

Contributors

Tassadaq Hussain, Mahmudur Rahman, Nuh Alpaslan, Abdelmoneim Sulieman, Edel Mendoza, Nadine Abi-Jaoudeh, Tsutomu Gomi

Notice

Statements and opinions expressed in the chapters are these of the individual contributors and not necessarily those of the editors or publisher. No responsibility is accepted for the accuracy of information contained in the published chapters. The publisher assumes no responsibility for any damage or injury to persons or property arising out of the use of any materials, instructions, methods or ideas contained in the book.

First published in London, United Kingdom, 2019 by IntechOpen
IntechOpen is the global imprint of INTECHOPEN LIMITED, registered in England and Wales, registration number: 11086078, The Shard, 25th floor, 32 London Bridge Street
London, SE19SG – United Kingdom
Printed in Croatia

British Library Cataloguing-in-Publication Data
A catalogue record for this book is available from the British Library

Additional hard and PDF copies can be obtained from orders@intechopen.com

Medical Imaging and Image-Guided Interventions, Edited by Ronnie A. Sebro
p. cm.
Print ISBN 978-1-83881-188-4
Online ISBN 978-1-83881-189-1
eBook (PDF) ISBN 978-1-83881-190-7

Meet the editor

Dr. Sebro completed his residency training at the University of California, San Francisco and fellowship training in musculoskeletal imaging and intervention at Massachusetts General Hospital. His Ph.D. in Biostatistics with a concentration in statistical genetics and theoretical statistics is from Harvard University. He is a former Howard Hughes Medical Institute (HHMI) Pre-Doctoral Fellow and a current Radiology Society of North America (RSNA) Research Scholar. Currently, his role at Penn Medicine includes the Director of Bone and Soft tissue Imaging and Intervention and is part of the Sarcoma Leadership Committee for the University of Pennsylvania Health System Abramson Cancer Center. Dr. Sebro's current research as a translational image-focused researcher centers on using novel PET tracers for prognosis and evaluation of response to therapy for bone and soft tissue sarcomas. Dr. Sebro has also been involved in several projects in musculoskeletal imaging of the knees, shoulder, and hips.

Contents

Preface

This edited volume is a collection of reviewed and relevant research concerning the developments in the field of medical imaging and image-guided interventions. It includes contributions from various international scholars, each edited by an expert in the related subject field. This book will be of use to scholars and specialists in medical imaging.

IntechOpen

Chapter 1

A High-Performance System Architecture for Medical Imaging

Tassadaq Hussain, Amna Haider,
Muhammad Shafique and
Abdelmalik Taleb-Ahmed

Additional information is available at the end of the chapter

http://dx.doi.org/10.5772/intechopen.83581

Abstract

Medical imaging is classified into different modalities such as ultrasound, X-ray, computed tomography (CT), positron emission tomography (PET), magnetic resonance imaging (MRI), single-photon emission tomography (SPECT), nuclear medicine (NM), mammography, and fluoroscopy. Medical imaging includes various imaging diagnostic and treatment techniques and methods to model the human body, and therefore, performs an essential role to improve the health care of the community. Medical imaging, scans (such as X-Ray, CT, etc.) are essential in a variety of medical health-care environments. With the enhanced health-care management and increase in availability of medical imaging equipment, the number of global imaging-based systems is growing. Effective, safe, and high-quality imaging is essential for the medical decision-making. In this chapter, we proposed a medical imaging-based high-performance hardware architecture and software programming toolkit called high-performance medical imaging system (HPMIS). The HPMIS can perform medical image registration, storage, and processing in hardware with the support of C/C++ function calls. The system is easy to program and gives high performance to different medical imaging applications.

Keywords: visual processing system, image processing, FPGA, embedded computer vision

1. Introduction

In medical imaging, high-performance graphics systems are being used for early diagnosing, planning treatment, and observing the problems. The medical imaging system plays

an important role in disease diagnostic time and cost. Therefore, to manage the industry demands, the medical health-care industry is looking for high-performance imaging system that can predict and identify the disease in an early stage without the support of an expert. As the performance of these devices grows, application-specific and high-performance hardware are required to run complicated/complex medical applications.

Precisely managing the medical information from multiple imaging equipment, processing them, and then displaying the result using various visual approaches give more detailed knowledge of understanding a disease state. The visual presentation performs multiple alignments and registration techniques using the complex and multi-dimensional images. The arrangement and registration of complex medical images having sparse data and control flow is a hard process. A medical imaging machine (e.g. radiological imaging) consumes 75% of processing time while aligning and registering, whereas a CT scan aligns images having a sample space of three-dimension with the reasonable isotropic resolution. These complex imaging applications have to follow anatomical and pathological structures while performing image acquisition, which demands efficient high-performance imaging hardware.

Medical imaging system uses different processing hardware such as reduced instruction set computer (RISC), application-specific instruction set processor (ASIP), single instruction multiple data (SIMD) processor, graphical processing units (GPUs), and field programmable gate arrays (FPGAs) [1, 2]. GPUs architecture uses advance vector processor architecture with dedicated memory and multiple stream multiprocessor (SM) having SIMD. The processing cores perform floating point operations. This high-end computing capability allows medical imaging applications to render complex medical images. In the past years, the GPU programming tools are grown and become competent in solving complex medical algorithm. On the other side, the performance of GPUs processing cores also increased, which allows medical imaging applications to give better results while diagnosing a problem.

Medical imaging is consistently held to be one of the most important advances in the history of medicine and has become an integral part of the diagnosis and treatment of patients around the globe. The medical statistic [3, 4] confirms that the early stage disease prediction, for example, breast, colorectal and lung cancers, etc., can save lives. This demands an improvement in diagnosis of the disease and screening techniques that generate high class, multidimensional images. With the development of medical imaging technology, the complexity of images also increased. It needs a high-performance computing architecture for real environment application processing. Existing medical imaging processing architectures face different issues and limitations related to hardware and software. Therefore, an efficient, scalable, and easily programmable high-performance medical imaging hardware architecture is required to solve complex imaging problems.

In this chapter, we proposed a high-performance medical imaging system (HPMIS) for medical applications. The proposed system works as a standalone device that processes images taken from different medical imaging equipment in real time. The HPMIS architecture is a

standalone heterogeneous system, which can perform image registration, storage, and processing in real-time environment. A software programming model is also proposed, which facilitates the medical scientists to write their imaging application without going into details of hardware. The proposed system is efficient in terms of performance and consumes low power due to the best utilization of hardware-software approach.

2. Related work

Imaging applications for clinical methods and pathology study need high performance and efficiency. Several image processing environments and processing architectures exist for the medical imaging application, but to the best of our information, a programmable and high-performance scalable processing system is required for medical imaging applications.

Ibanez et al. [5] designed an open-source medical imaging toolkit called the Insight Toolkit (ITK). The developed toolkit supports a number of platforms and gives programmers with an extended C++ framework of software tools for image understanding.

Schroeder et al. [6] developed an open-source Visualization ToolKit (VTK) for three-dimensional processing and visualization. VTK toolkit assists C++ libraries and algorithms for different parallel processing technologies and provides an interface to integrate with different databases.

Wolf et al. [7] introduced Medical Imaging Interaction Toolkit (MITK) that assists to program medical image-based clinical software. The MITK gives an application programming framework that links with the ITK and the VTK libraries. The proposed HPMIS provides a medical imaging programming model, which supports data registration, memory management, and processing in hardware, and is easy to program. The HPMIS programming model is scalable for different architectures having reduced instruction set computing (RISC) multi-processors, application specific hardware cores, and vector processors.

Bakalash et al. [8] suggested the MediCube system for 3D medical imaging. The system gives the reconstruction and visualization of three-dimension complex medical images. The processing system of the MediCube uses a RISC processor that performs the parallel processing for real-time voxel representation, whereas the HPMIS handles 3D medical imaging using a specialized local memory system and uses reconfigurable processing cores to process the incoming data. Bluetechnix [9] Black camera boards use specialized DSP processors and provide excellent image processing abilities at the expense of power, price, and complexity. Lee et al. [10] proposed a SONY DSP processing-based system.

Jinghong et al. [11] proposed image processing system having heterogeneous (DSP and FPGA) processing cores. The HPMIS uses FPGA accelerators for high-speed data acquisition from single or multiple sensors. The HPMIS processing architecture uses multi-processor core architecture, each core using 32-bit RISC instruction set architecture (ISA) is integrated with the design for programmability, average performance, and low-cost systems.

Pratx et al. [12] proposed a method for processing line-projection tasks to process the PET image reconstruction. The proposed method uses Nvidia processing cores and the CUDA programming model. Owens et al. [13] addressed the implementation of RISC processors on GPU cores-based processing system architecture. The authors showed the value of GPU for the tremendous compute capacity that reproduces the CT images and presents them on screen.

Jiang et al. [14] suggested processing of 3D discrete transformation using hardware accelerator. The proposed system decreases the size of the accelerators lookup tables. The accelerators are developed in hardware description language and examined on Xilinx Virtex-E FPGA board.

Coric et al. [15] displayed a CT-based parallel beam back-projection algorithm and tested on FPGA-based hardware architecture. The FPGA-based system obtains the speedups up to 100× against the software running on a 1 GHz Pentium.

Tassadaq et al. proposed programmable graphics controller [16, 17] for low-cost and low-power graphics system. The system takes two-dimensional images to process applications. Tassadaq et al. [18] also have proposed a visual processing system called ViPS for medical applications. The ViPS uses multiple RISC, vector processor, and multiple FPGA-based hardware accelerators. The ViPS gives a high performance by using advanced hardware architectural support such as registration system, memory system, and processing system.

3. High-performance medical imaging system

Imaging has become an essential tool in modern medicine science. Numerous powerful platforms to register, store, analyze, and process medical imaging applications have appeared in recent years. However, these systems are developed for a specific imaging application problem [19–21] and do not support generalized problems [22], which includes an indigenous system that could be customized according to the local needs. Moreover, the cost of such systems is on higher side that contributes to the increase in expenses of each scan. This results in discouraging patients, who could not afford these high costs and therefore compromise on their health. Also, in many medical imaging systems such as MRI, temporal resolution has been reported to be a major concern, which causes discomfort to patients with severe illness/pain as they have to be motionless for a longer period of time. In this chapter, a high-performance medical imaging system (HPMIS) is proposed that registers stores and processes complex and multidimensional medical imaging application in real-time. The high-performance medical imaging system provides a user-friendly programming environment and high-performance architecture to perform imaging data acquisition, registration, storage, analysis, and performs segmentation, filtering, and recognition for complex real-time complex and multidimensional medical images or videos. The proposed system is highly reliable concerning cost, performance, and power. High-performance medical imaging system architecture (shown in **Figure 1**) is implemented and tested on advanced heterogeneous multi-core and GPU-based systems.

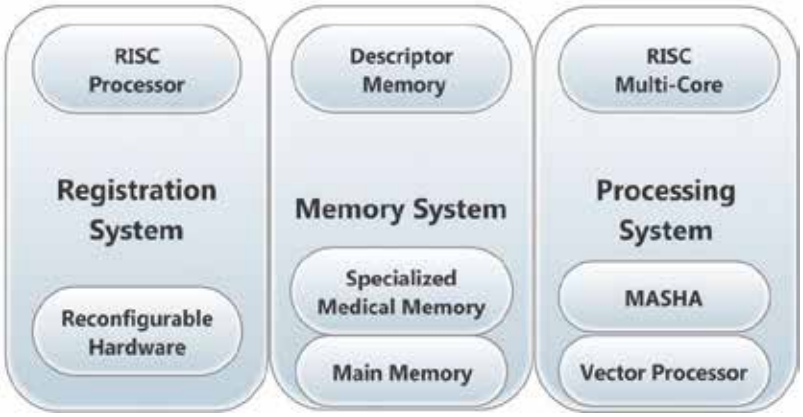

Figure 1. High-performance medical imaging system.

The proposed high-performance medical imaging system (HPMIS) has five sub systems: registration system, memory system, processing system, programming toolkit, and test applications.

3.1. Registration system

The registration system (RS) deals with a number of medical imaging devices with various interfaces. The RS supports multidimensional and scattered graphics data. The RS manages X-ray radiography, ultrasonic images, etc. and complex images such as MRI, CT, etc. The RS utilizes a RISC core and FPGA accelerator to access data from medical imaging devices. The RISC core is employed to obtain medical images having a complex structure, whereas the FPGA core is used to gather data having fixed data flow patterns. The registration system aligns images reasonably isotropic resolution and do not distort or deform the anatomical and pathological structures of images. The system is designed for navigation and visualization of multimodality and multidimensional images for 2D/3D, 4D Cardiac-CT and 5D Cardiac-PET-CT displays. The registration system supports all DICOM Files (mono-frame, multi-frames), the MRI/CT multi-frame format, JPEG Lossy, Lossless, LS and 2000, RLE, Monochrome1, Monochrome2, RGB, YBR, Planar and Palettes. The system supports 32-bit pixel resolution and is directly linked with memory system.

3.2. Memory system

The HPMIS memory system uses three types of memories: the program memory, the specialized medical memory, and the main memory. The HPMIS program memory utilizes the memory access descriptors [APMC][PPMC][PMC] that contain the knowledge of imaging data registration, data transfers, storage device, and processing cores. The descriptors provide the medical imaging programmer to choose a processing core for image processing and explain the complicated image structure.

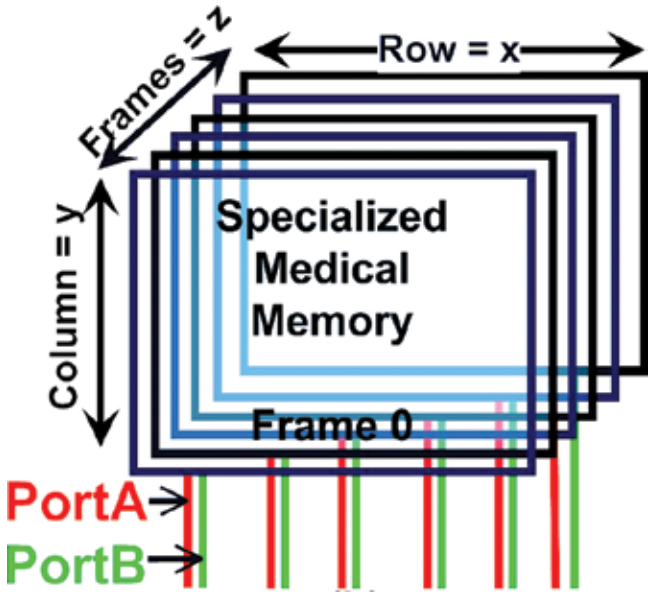

Figure 2. High-performance specialized medical memory.

3.2.1. High-performance specialized imaging memory

The HPMIS high-performance specialized imaging memory (shown in **Figure 2**) is directly connected to the processing system and provides single cycle data access. The high-performance specialized imaging memory holds the complex medical image data pattern to speed up the data transfer accesses. The high-performance specialized imaging memory has parameterizable and programmable 3D memory structure. Depending upon the available on-chip memory, the high-performance specialized medical memory can be organized into multiple frames. To exploit parallelism better, the frames of high-performance specialized medical memory are arranged physically into a multi-dimensional (1D/2D/3D) architecture to map the kernel access pattern on the high-performance specialized imaging memory.

3.2.2. Main memory

The slowest type of memory in the HPMIS architecture is main memory and is accessible by the whole system. The main memory has SDRAM, SD/SDHC memories, etc. interfaces to read/write data.

3.2.3. Permanent memory

The permanent memory of high-performance medical imaging system is used to store dense and large size of medical images in a nonvolatile memory permanently.

3.3. Processing system

The processing system is used to perform image processing on images stored in memory system. The medical application-specific hardware accelerator, vector processor, and the multi RISC processor cores are used in the HPMIS processing system.

3.4. Programming

The HPMIS Medical Application Programming Model (MAPM) helps medical application programmers to develop applications without acknowledging hardware arrangements and details. The MAPM uses image processing functions for image segmentation, reconstruction, features extraction, and computation; and it also provides memory management and registration task and separate task for visualization. The MAPM presents various function calls, which include medical imaging flow, control, and processing. The MAPM data transfer tasks help disordered, random, strider 1D, 2D, 3D, and automated blocking for image/video transfer processes and move data between the medical imaging devices and the HPMIS memory system. The HPMIS MAPM intelligently pipeline, overlap, and parallelize image processing tasks based on hardware processing and memory resources. **Table 1** presents functions that are used to develop the applications for the HPMIS architecture. The HPMIS incorporates 100 function calls for medical applications. The application calls are written in C/C++. The function allows the programmer to execute the function on RISC or Vector processors.

API Function	Description
Registration calls	Description

`MSD,`
`NCA,`
`Sample,`
`NN,`
`3D_FILTER(`
`SPECIALIZED_MEMORY,`
`DATA_SET, Kernel, Priority)`
	Applies Means Square Difference
	Normalized Correlation Coefficient
	Down/Up Sampling
	Applies Nearest Neighbourhood
	Specialized Data Transfer
	`MEDICAL_MEMORY` indicates SMM structure
	`DATA_SET` indicates *Main Memory* data set
	Kernel defines the type of filter

Storage calls	

`READ_IMAGE, WRITE_IMAGE,`
`ViPS_MEMCPY (`
`MEDICAL_SENSOR,`
`SPECIALIZED_MEDICAL_MEMORY,`
`DATA_SET, Priority)`
	Image Data Access
	`IMAGE_SENSOR` defines medical sensor to read data
	`SPECIALIZED_MEDICAL_MEMORY` or `DATA_SET`
	indicates complex *Local Memory* or
	external *Main Memory* to place data

Processing calls	

`PROCESSING(`
`CORE,`
`DATA_SET, Priority)`
	Processing Task
	`CORE` indicates the Processor
	(MASHA, Vector or RISC) Core

Table 1. C/C++ device drivers to program/operate HPMIS.

3.5. Test applications

To validate the HPMIS system, different medical applications are executed. The medical applications includes segmentation, K-mean clustering, object detection, object recognition, features extraction, 3D-Stereo filtering, ultrasonic image reconstruction, time domain filtering, frequency domain filtering, alpha blending, and Iris-based disease recognition.

4. Results

The high-performance medical imaging system is tested with the test applications discussed in Section 3.5. The results show that HPMIS-based architecture draws low power and gives high performance for the test applications. While executing test application on multi-RISC and FPGA cores of HPMIS, the results show that the HPMIS FPGA-cores improve the application performance 2.4 times compared to multi-core RISC system. The HPMIS performs real-time complex images reconstruction at higher rate.

5. Conclusion

In this chapter, we have introduced and developed a high-performance medical imaging system (HPMIS) for medical imaging applications. The HPMIS has the capability to register multi-dimensional, complex, and high-resolution images, and processes the application on different heterogeneous multi-core processors. The HPMIS system gives efficient imaging access from multiple medical equipment. The HPMIS provides a medical programming environment that includes different function calls for the development of medical imaging application. The programming environment provides the data structure to present medical images or videos.

Author details

Tassadaq Hussain[1,2]*, Amna Haider[1,2], Muhammad Shafique[1]
and Abdelmalik Taleb-Ahmed[3,4,5]

*Address all correspondence to: tassadaq@ucerd.com

1 Riphah International University and UCERD Islamabad, Islamabad, Pakistan

2 UCERD, Islamabad, Pakistan

3 Laboratory of Industrial and Human Automation, Mechanics and Computer Science, France

4 ASHM–Automatic Control and Human-Machine Systems, France

5 Université de Valenciennes et du Hainaut Cambrésis Bat Malvache, France

References

[1] OGRE: Object-Oriented Graphics Rendering Engine. http://www.ogre3d.org/

[2] Alzaabi A et al. Tcct: A GUI table comparison computer tool. In: Emerging Trends in Computing, Informatics, Systems Sciences, and Engineering. Springer; 2013

[3] Siegel R, DeSantis C, Jemal A. Colorectal cancer statistics. CA: A Cancer Journal for Clinicians. 2014;**64**(2):104-117

[4] Siegel RL, Miller KD, Jemal A. Cancer statistics, 2016. CA: A Cancer Journal for Clinicians. 2016;**66**(1):7-30

[5] Ibanez L, Schroeder W, Ng L, Cates J. The Itk Software Guide; 2003

[6] Schroeder WJ, Avila LS, Hoffman W. Visualizing with vtk: A tutorial. Computer Graphics and Applications, IEEE. 2000;**20**(5):20-27

[7] Wolf I, Vetter M, Wegner I, Nolden M, Bottger T, Hastenteufel M, et al. The medical imaging interaction toolkit (mitk): A toolkit facilitating the creation of interactive software by extending vtk and itk. In: Medical Imaging 2004, Pages 16-27. International Society for Optics and Photonics; 2004

[8] Bakalash R, Kaufman A. Medicube: A 3d medical imaging architecture. Computers & Graphics. 1989;**13**(2):151-157

[9] Bluetechnix Black DSP. http://www.xbow.com

[10] June-Sok L, Jung Y-Y, Kim B-S, Ko S-J. An advanced video camera system with robust AF, AE, and AWB control. IEEE Transactions on Consumer Electronics. 2001;**47**(3):694-699

[11] Jinghong D, Yaling D, Kun L. Development of image processing system based on DSP and FPGA. In: Electronic Measurement and Instruments; 2007. ICEMI'07

[12] Pratx G, Cui J-Y, Prevrhal S, Levin CS. 3-d tomographic image reconstruction from randomly ordered lines with cuda. W. Mei Hwu (Morgan Kaufmann, San Francisco, CA 2011). pp. 679-691

[13] Owens JD, Luebke D, Govindaraju N, Harris M, Krüger J, Lefohn AE, Purcell TJ. A survey of general-purpose computation on graphics hardware. In: Computer Graphics Forum. Vol. 26. Wiley Online Library; 2007. pp. 80-113

[14] Jiang RM, Crookes D. Fpga implementation of 3d discrete wavelet transform for real-time medical imaging. In: Circuit Theory and Design, 2007. ECCTD 2007. 18th European Conference on. IEEE; 2007. pp. 519-522

[15] Coric S, Leeser M, Miller E, Trepanier M. Parallel-beam backprojection: An fpga implementation optimized for medical imaging. In: Proceedings of the 2002 ACM/SIGDA Tenth International Symposium on Field-Programmable Gate Arrays. ACM;2002. pp. 217-226

[16] Hussain T, Palomar O, Cristal A, Unsal O, Ayguady E, Valero M, et al. Stand-alone memory controller for graphics system. In: The 10th International Symposium on Applied Reconfigurable Computing (ARC 2014). ACM; 2014

[17] Hussain T, Haider A. PGC: A pattern-based graphics controller. The International Journal of Circuits and Architecture Design. 2014

[18] Hussain T, Palomar O, Cristal A, Ayguadé E, Amna H. HPMIS: Visual processing system for medical imaging. In 2015 8th International Conference on Biomedical Engineering and Informatics (BMEI). Vol. 43(4), 1998. IEEE; 2015. pp. 40-45

[19] Flannery BP et al. Three-dimensional X-ray microtomography. Science. 1987;**237**(4821): 1439-1444

[20] Liang Z-P, Lauterbur PC. Principles of Magnetic Resonance Imaging: A Signal Processing Perspective. SPIE Optical Engineering Press; 2000

[21] Khadivi KO. Computed tomography: Fundamentals, system technology, image quality, applications. Medical Physics. 2006;**33**:8, 3076-3076

[22] Sakamoto T. Medical image processing apparatus, medical image processing method, and medical image processing system. U.S. Patent Application 10/002,423, filed. 19 June 2018

Chapter 2

A Decision Support System (DSS) for Breast Cancer Detection Based on Invariant Feature Extraction, Classification, and Retrieval of Masses of Mammographic Images

Mahmudur Rahman and Nuh Alpaslan

Additional information is available at the end of the chapter

http://dx.doi.org/10.5772/intechopen.81119

Abstract

This paper presents an integrated system for the breast cancer detection from mammograms based on automated mass detection, classification, and retrieval with a goal to support decision-making by retrieving and displaying the relevant past cases as well as predicting the images as benign or malignant. It is hypothesized that the proposed diagnostic aid would refresh the radiologist's mental memory to guide them to a precise diagnosis with concrete visualizations instead of only suggesting a second diagnosis like many other CAD systems. Towards achieving this goal, a Graph-Based Visual Saliency (GBVS) method is used for automatic mass detection, invariant features are extracted based on using Non-Subsampled Contourlet transform (NSCT) and eigenvalues of the Hessian matrix in a histogram of oriented gradients (HOG), and finally classification and retrieval are performed based on using Support Vector Machines (SVM) and Extreme Learning Machines (ELM), and a linear combination-based similarity fusion approach. The image retrieval and classification performances are evaluated and compared in the benchmark Digital Database for Screening Mammography (DDSM) of 2604 cases by using both the precision-recall and classification accuracies. Experimental results demonstrate the effectiveness of the proposed system and show the viability of a real-time clinical application.

Keywords: breast cancer, mammogram, NSCT, HOG, classification, diagnostic aid, computer-aided diagnosis (CAD), content-based image retrieval

1. Introduction

Breast cancer is considered a major health problem since it is the second most common cause of cancer among women only after lung cancer in both developed and developing countries [1, 2]. Based on the estimates of American cancer society (ACS), there were 231,840 new cases of invasive breast cancer and 40,290 breast cancer deaths among U.S. women in 2015 [3]. Although, the breast cancer mortality has declined among women of all ages during the last two decades due to the result of treatment improvements, earlier detection, and awareness, the incidence rate has increased significantly during this time [2, 3].

The diagnosis and detection of breast tumor in the early stages is the best opportunity to increase the chances of survival. Therefore, women of age 40 or older are recommended to get mammograms regularly. However, such a recommendation results in the generation of a very large number of mammograms that need to be processed. In addition, the interpretation of mammogram images mostly depends on the experience of the radiologists, and the tumors may be overlooked easily while viewing the image in early stages of breast cancer as the clinical indications are varied in appearance [4]. Screening mammograms is also a repetitive task that causes fatigue and eye strain since for every thousand cases analyzed by a radiologist, only 3–4 are cancerous and thus an abnormality may be overlooked [5]. It has been seen that between 60 and 90% of the biopsies of cancer cases predicted by radiologists found benign later and those biopsied women are exposed to needless fear and anxiety [6].

To support radiologists in the process of visually screening mammograms to avoid miss-diagnosis, computer-aided detection and/or diagnosis (CADe and CADx) systems have been proposed for analyzing digital mammogram due to the rapid advancement of digital imaging, computer vision, pattern recognition and machine learning technologies [7–9]. The CADe systems are responsible for highlighting or cueing the locations depicting the suspicious micro calcification clusters and masses and CADx systems deal with classifying classification between malignant and benign masses. Many methods have been proposed in the literature to assist radiologists in accurate interpretation of mammogram for detection of suspicious areas of micro-calcification clusters and breast masses often hidden in dense breast tissues and classification to benign and malignant lesions utilizing a wide variety of algorithms [10–15]. Previous studies have shown that using CAD improves radiologists' efficiency in searching for and detecting micro-calcification clusters as well as helps them detect more cancers associated with malignant micro-calcifications [10]. However, current CAD has no or little impact in helping radiologists detect more subtle cancers associated with mass-like abnormalities due to the relatively low performance in mass detection due to large variation in shape and size and are often indistinguishable from surrounding tissues [15].

Also, the majority of the research efforts in this domain has focused on the problem of the cancer detection, in which the likelihood of malignancy is computed based on some feature extraction and classification schemes [15–19]. These systems are non-interactive in nature and the prediction represents just a cue for the radiologist without the ability to explain the reasoning of the decision-making (the "black-box" type approach), as the final decision regarding the likelihood of the presence of a malignant mass is left exclusively to him/her. Hence, the clinical benefit of using current commercially available CAD systems is still under debate and test.

In the last several years, developing CAD schemes that use content-based image retrieval (CBIR) approach to search for the clinically relevant and visually similar mammograms (or regions) depicting suspicious lesions has also been attracting research interest [20–22]. CBIR-based CAD schemes have potential to provide radiologists with "visual aid" and increase their confidence in accepting CAD-cued results in the decision making. Furthermore, CBIR would be a useful aid in the training of students, residents, and less experienced radiologists since it would allow them to view images of lesions that appear similar, but may have differing pathology and help them see how the pattern in their current case closely resembles a pattern in cases previously proven to be non-cancerous, thereby, improving specificity. Although preliminary studies have suggested that using CBIR might improve radiologists' performance and/or increase their confidence in the decision making, this technology is still in the early development stage with lack of benchmark evaluation in ground-truth datasets. Despite of great research interest and the significant progress made in the last several years, developing CBIR approaches for breast cancer detection that can be routinely accepted and applied in the clinical practice is still not a reality.

To address the limitation of the current CAD in detecting mass-like abnormalities and due to the ongoing success of CBIR to provide clinical decision support for medical images of different modalities, we proposed to develop an integrated and interactive retrieval system. It will be able to respond to image based visual queries of automatically segmented suspicious mass region by displaying mammograms of relevant masses of past cases that are similar to the queried region as well as predicting the image categories (e.g., malignant, benign and normal masses). The performance and reliability of such a CBIR system depends on a number of factors (or issues) including the optimization of lesion segmentation, feature extraction, classification, similarity measures and relationship between the clinical relevance and visual similarity, database quality and sizes.

The most challenging problem in this task is detecting the mass from the background and extracting the discriminative local features of clinical importance. A Graph-Based Visual Saliency (GBVS) method [23] is utilized for the segmentation of the regions of interest (ROIs) as breast masses. To extract invariant features from masses, Non-Subsampled Contourlet transform (NSCT) [24] is utilized due to its powerful capability in image representation compared to wavelets and contourlet transform. Furthermore, in order to distinguish normal and abnormal tissues, eig(Hess) HOG [25] features are extracted based on computation of eigenvalues of the Hessian matrix in a histogram of oriented gradients in addition to several geometric features from the masses in mammographic images. HOG is known as a keypoint descriptor in literature which expresses the local statistics of the gradient orientations around a keypoint [46]. The HOG feature can express object appearance due to the reason that the histogram process gives translational invariance the gradient orientations are strong to lighting changes. It is also useful for the classification and retrieval of textured breast masses with different shapes.

For classification, two-class separation (normal and abnormal) and three-class study (normal, benign, and malignant cases) are carried out on the individual and combined input feature spaces by utilizing Support Vector Machines (SVM) and Extreme Learning Machines (ELM) with 10-fold cross validation. For retrieval, performances are evaluated and compared in different feature spaces in the benchmark DDSM dataset [26] using precision and recall curves

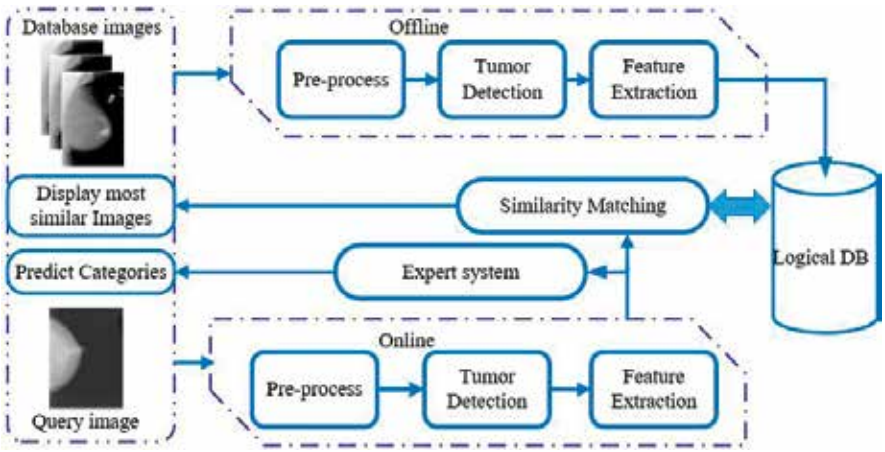

Figure 1. Dataflow diagram of the integrated decision support system (DSS).

obtained from comparison between the query and retrieved images. The system performance is compared with other state-of-the-art algorithms where experimental results indicate that the framework achieved a noticeable increase in recognition rates.

Figure 1 shows the dataflow diagram of the proposed integrated decision support system based on image pre-processing, mass segmentation, feature extraction, classification, and retrieval.

The rest of the paper is organized as follows. Section 2 describes the related works, specially talk about the CAD-based CBIR systems for mammographic mass retrieval. The mass detection based on marker-controlled watershed segmentation and feature extraction are described in Sections 3 and 4 respectively. Our classification and similarity matching methods are described in Section 5, while all discussions on the obtained experimental results are given in Section 6. The last section comprises of conclusions.

2. Background review

There is a clear need to create effective tools and techniques to search, browse and retrieve images from large repositories to aid diagnoses and research due to the phenomenal growth in recent years in the volume of digital mammograms produced in hospitals and clinical centers. Due to the freely available access to datasets of digital mammograms, such as the Digital Database for Screening Mammography (DDSM), interest in developing CAD schemes for mammograms that use CBIR has been attracting continued research interest during the last several years [20–22]. Although mammography-based CAD is one of the mature and widely adopted fields, there have been only a limited number of studies devoted to CBIR-based CAD systems for the detection and retrieval of breast masses in mammograms. Alto et al. [21] proposed the use of the shape, gradient, and texture features for mammography image retrieval

and that was one of the earliest researches on CBIR for mammograms. Linear discriminant analysis, logistic regression, and the Mahalanobis distance were used to evaluate the features for classifying the masses. Kinoshita et al. [22] used the breast density to retrieve images from a mammogram dataset available at the Clinical Hospital of the University of São Paulo at Ribeirão Preto, Brazil. Shape, texture features, moments, Radon transform, and histograms were used to describe breast masses, and the Kohonen self-organizing map (SOM) neural network was used for image retrieval. Wang et al. [27] has utilized histograms for the characterization of breast mass in a set of mammogram database at the Medical Center of Pittsburgh in order to automatically evaluate breast mass. They obtained 71% of correct classification rate with the use of a neural network. Muramatsu et al. [28] proposed a psychophysical similarity measure based on neural networks for evaluation of similar images with mammographic masses. The major drawback is that a large amount of data is required to train an artificial neural network (ANN). Oliveira et al. proposed a CBIR system called MammoSys; the novelty of this study is to present a two-dimensional principal component analysis (2DPCA) method [29] for the description of mass texture and thereby also a dimensionality reduction is performed. Wei et al. [30] proposed an adaptive classification scheme in the context of SVM assisted by content-based image retrieval to improve the classification accuracy in the computer aided diagnosis for breast cancer. A CBIR scheme is proposed in [31] that utilizes SVMs capable of optimally exploiting the distribution of input samples in the feature space on the basis of BI-RADS classifications of masses as carried out by the radiologists. In an article by Zhang [20], a number of CBIR-based CAD schemes for mammograms were compared and their performance were assessed and it was concluded that much research work is needed before the CBIR-based CAD schemes can be accepted in the clinical practice.

3. Breast mass detection

The most challenging aspect in developing any CAD based systems for mammograms is to segment the suspicious masses, which are often hidden in dense breast tissues. Since a cancerous region might typically represented by local-oriented patterns, accurately segmenting it is an important first step for the effective performances of the successive feature extraction, similarity matching and classification steps in developing a CAD system as shown in **Figure 1**. A large number of segmentation methods have been proposed in the literature for the detection of breast masses, such as adaptive region growth [32], multi-layer topographic region growth algorithm [33], active contour (snake) modeling [34], level set algorithm [35], dynamic programming [36] etc. However, due to the limitation of benchmark evaluation and testing datasets to compare the performances, it is difficult to find the most robust and effective method in this domain till now.

3.1. Visual saliency based segmentation

The breast anatomy has a complicated structure because of the presence of pectoral muscles and the different mass density. Although it is easy to analyze breast tissues without getting

confused with pectoral muscles for a radiologist, it is always difficult to distinguish between pectoral muscles and mass for an automatic method in a CAD system. For that reason, pectoral muscles are removed usually before the segmentation, which has a huge limitation as it is done manually in most cases [8, 15, 19]. However, automatic segmentation of pectoral muscle is a troublesome process and also an additional workload in analysis of mammography images in cranio-caudal (CC) view, which are generally without pectoral muscles.

In this study, for example a graph-based visual saliency (GBVS) method [37] is utilized for segmentation by applying thresholding on the saliency map, which does not require the removal of pectoral muscles to detect the breast masses. The reason for choosing GBVS is that it has the ability of generating an output showing concentrated saliency maps in the appropriate image regions where the value of an image pixel location corresponds to the saliency of that pixel with respect to the neighbors. The usefulness of saliency models in cases where some structures are implicit with respect to the image such as pectoral muscles in mammograms is demonstrated in [19]. It is also experimentally shown that the GBVS yields the best results for mass detection from screening mammograms [37].

The GBVS calculates the saliency of a region with respect to its local neighborhood using the directional contrast. In mammography images, it has been monitored that the contrast of mass containing regions is significantly different from the remaining breast tissue. As discussed earlier, the mass encircled by dense tissues is difficult to recognize, whereas, the directional contrast with respect to the local neighborhood helps in identifying such masses along with the masses present in fatty regions. The computation of saliency map consists of following stages: Firstly, to differentiate mass from the neighboring regions in contrast, feature maps are computed from contrast values along four different orientations of 2D Gabor filters (0°, 45°, 90°, and 135°). Then, activation maps are computed as the balanced distribution of a Markov chain which is obtained using the initial feature maps [20]. The balanced distribution denotes higher weights only for the edges present in salient regions. The Ergodic Markov chains are modeled on a fully connected directed graph obtained from feature maps. Weighted connections are used to create the graph. It is created by connecting nodes in a feature map. The directed edge node (i, j) to node (k, l) weight is assigned in the graph.

$$w\big((i,j),(k,l)\big) \overset{\mathrm{A}}{=} D \cdot F(i-k, j-l), \tag{1}$$

where $F(a,b) \overset{\mathrm{A}}{=} \exp\left(-\frac{a^2+b^2}{2\sigma^2}\right)$

$$\mathrm{D} \overset{\mathrm{A}}{=} \left|\log\left(\frac{M(i,j)}{M(p,q)}\right)\right| \tag{2}$$

where $M(i, j)$ denotes a node in the feature map and σ is set to 0.15 times the image width.

Due to the fact that activation maps lack the accumulation of weights, a normalization of activation map is performed to avoid uniform saliency maps. Activation maps are normalized using a similar approach as used in the previous step. Markov chains are computed from the

http://dx.doi.org/10.5772/intechopen.81119

activation maps. The function D in Eq. (2) maps to the value at location (k, l) in activation map (Eq. (5)). The value of the parameter σ in Eq. (1) is 0.06 times the image width [38].

$$D \overset{A}{=} A(p, q) \tag{3}$$

where $A(p, q)$ represents a node in the activation map. In final stage, normalized activation maps are combined using the sum rule to obtain the saliency map. Once the saliency map

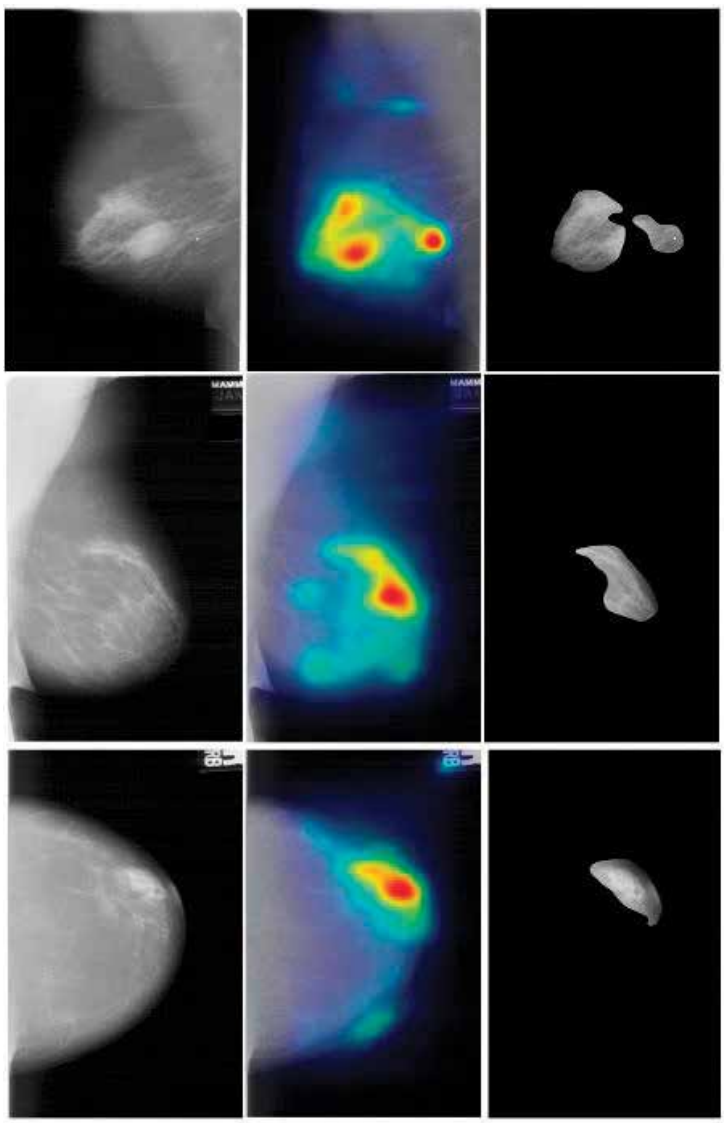

Figure 2. Saliency map generated from enhanced image and suspicious regions obtained after thresholding.

is computed, a threshold is empirically selected to obtain the optimal size ROIs. **Figure 2** illustrates some examples of saliency maps generated from pre-processed images and ROI segmentation from the saliency maps.

4. Feature extraction

Feature extraction plays key role in our breast cancer diagnosis framework. Feature extraction process can only be carried out if the suspicious areas of breast masses are appropriately defined. In selecting effective features from mammogram lesions, great research efforts have been focused on capturing the texture of images and improving correlation to the human visual similarity. Among them, Curvelet transform, Gabor Wavelet, Discrete Wavelet Transform (DWT), and Spherical Wavelet Transform (SWT), Contourlet Transform (CT), local binary pattern (LBP) have been extensively investigated and compared in addition to other popular texture features derived from the co-occurrence matrices and Fourier transformation [39–44]. Since, clinically and visually similar lesions or disease patterns can depict on different locations of the mammograms with different orientations, the selected features should be invariant to the linear shift and rotation of the targeted lesions. To consider these criteria, NSCT and HOG based approaches are used for feature extraction in addition to traditional shape, mass and GLCM based features from region-of-interests (ROIs) with adaptively adjusted size based on the actual mass region segmentation results.

4.1. Non-subsampled contourlet transform

Despite different applications of Wavelet Transform in medical image analysis, it has some limitations in capturing the directional information in images such as smooth contours and the directional edges. For example, orthogonal wavelets consider only horizontally, vertically, and diagonally directed discontinuities. These directions do not express effectively the edges and textures of medical images such as breast mammograms, which have smooth curves that represent benign, malignant masses and micro-calcifications, etc. To express the contour-like smooth edges directly in the discrete domain effectively, the Contourlet Transform was introduced by Do and Vetterli [45], which is an extension of the wavelet transform which uses multi scale transform that is constructed by combining the Laplacian pyramid with directional filter banks (DFB) and has additional characteristics such as directionality and anisotropy in addition to the properties of Wavelet Transform. Although the Contourlet Transform is a more effective method than the Wavelet Transform in image representation, it is not shift-invariant due to down-sampling and up-sampling. Non-Subsampled Contourlet Transform (NSCT) was proposed by Cunha et al. [21] to compensate this limitation and due to its beneficial features, the NSCT has been used in this work for representing the breast masses according to its features.

In NSCT, to keep away from the frequency aliasing of the CT and to obtain the shift-invariance, the non-subsampled Laplacian Pyramids (NSLP) and the non-subsampled directional filter banks (NSDFB) is utilized based on Idealized frequency partitioning obtained with

the structure proposed in [21]. Additionally, the multi-scale and directional decomposition processes are free from each other. The number of decomposition directions is changeable and can be adjusted to any value of 2^{l_j} where the l^j parameter can be represented at scale j, $1 \leqslant j \leqslant J$ and J represents the number of decomposition scales. Different from the classical CT, all subbands of NSCT have the same resolution. That means, the NSCT coefficients of each subband are in one-to-one correspondence with the original surface in the spatial domain. For feature extraction, a combination of k mean, variance, energy, entropy, skewness, and kurtosis parameters from 4-level non-sampled contourlet transform is examined. An example of the NSCT for a mass is shown in **Figure 3**. The image is decomposed into four pyramidal levels, resulting in one, two and eight sub-bands.

4.2. Eig(Hess)-HOG features

The HOG is computed for each key point from a block. The key point denotes the center of the central cell of the block. The adjacent area of each key point is partitioned into cells. One-dimensional histogram of gradient orientations is accumulated for each cell. The histogram of all the cells generates the feature of all key points [22, 46]. A simple 1-D $[-1; 0; 1]$ mask is used

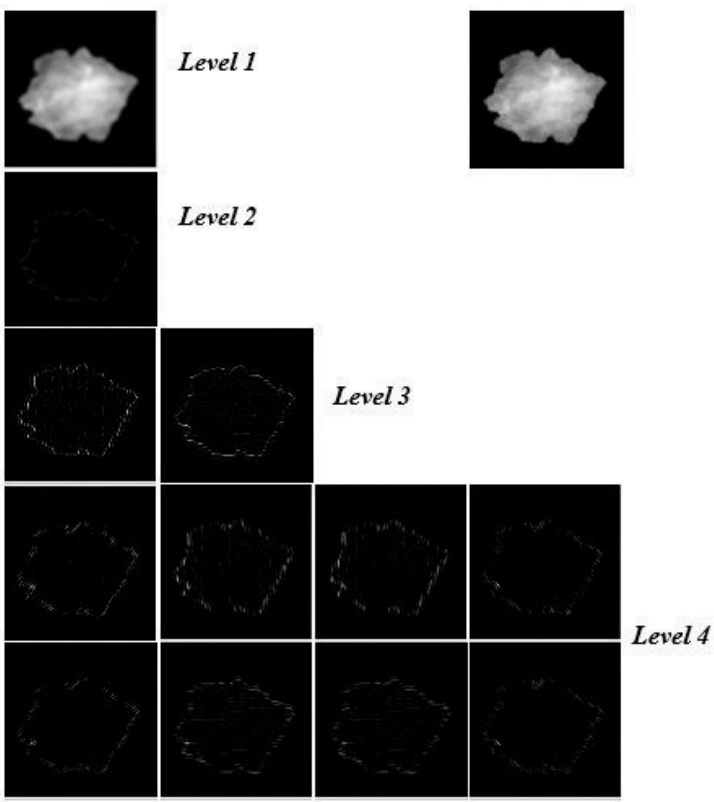

Figure 3. Non-sampled Contourlet transform of an ROI with four-level decomposition.

for the gradient computation. In conventional HOG, firstly the grayscale image is filtered with mask to obtain x and y derivatives of image as in Eq. (4).

$$\begin{aligned} f_x(x,y) &= I(x+1,y) - I(x-1,y) \quad \forall x,y \\ f_y(x,y) &= I(x,y+1) - I(x,y-1) \quad \forall x,y \end{aligned} \tag{4}$$

where f_x and f_y indicates x and y derivatives of image gradient. $I_{(x,y)}$ indicates the intensity at position$_{(x,y)}$. The magnitude and orientation is calculated as in Eq. (5) and (6);

$$m(x,y) = \sqrt{f_x(x,y)^2 + f_y(x,y)^2} \tag{5}$$

$$\theta(x,y) = \tan^{-1}\left(\frac{f_y(x,y)}{f_x(x,y)}\right) \tag{6}$$

The gradient orientations are partitioned into eight bins. For each pixel's orientation bin, the orientation's magnitude $m(x,y)$ is voted to each bin. Then, orientation histogram of every cell and spatial blocks are normalized.

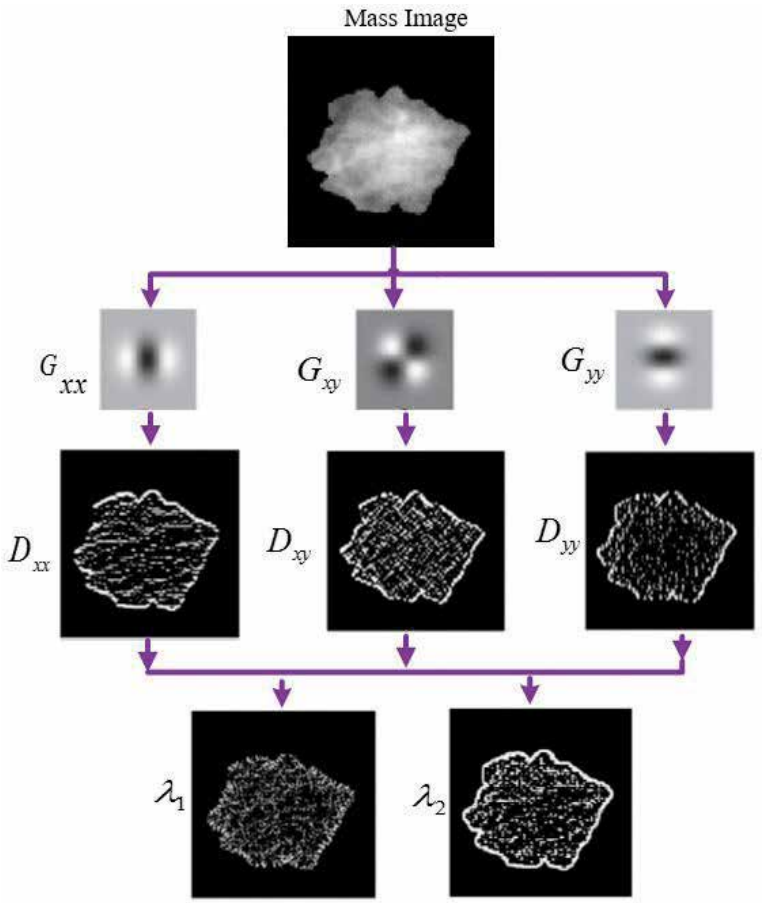

Figure 4. Computation of eigenvalues of the hessian matrix for an ROI as breast mass.

http://dx.doi.org/10.5772/intechopen.81119

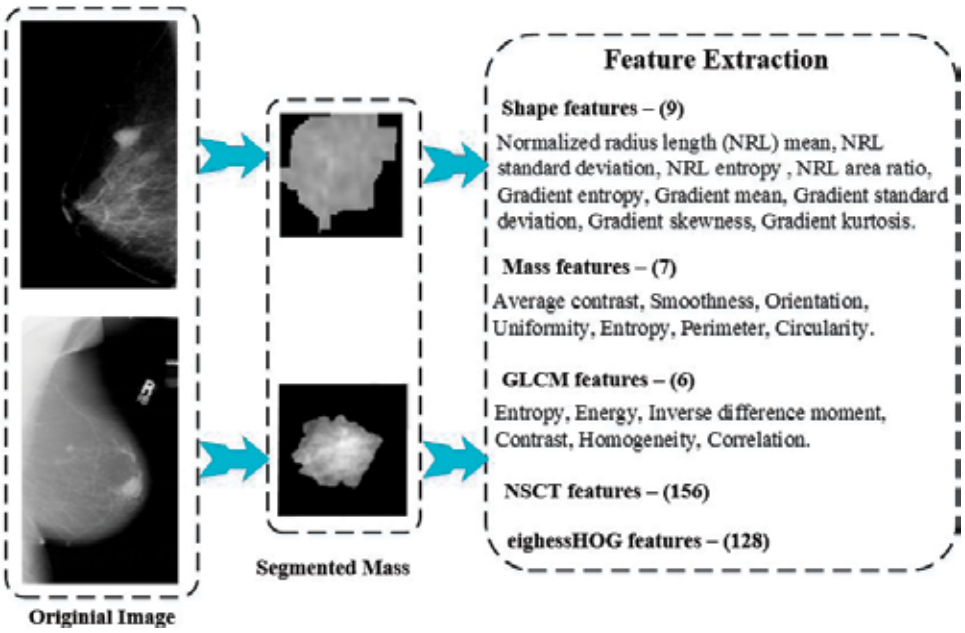

Figure 5. Feature extraction stage with an example mammogram.

Eig(Hess)-HOG uses the Hessian matrix instead of the Gaussian derivative filters to compute the eigenvalues of image surface. The Hessian matrix contains more differential information than the conventional gradient. The Hessian matrix of an image is defined as the second-order partial derivative matrix of the gray scale image. The second order differentials provide more accurate analysis in detail about function curves in breast masses [22].

The number of possible orientation bins is referred to as N_o and the number of cells for direction is referred to as N_c. We set the parameters of the descriptor to $N_c = 4$ cells and $N_o = 8$ bins resulting in a total of $N_o \times N_c^2 = 128$ elements in a HOG feature. **Figure 4** demonstrates the computation of eigenvalues of the Hessian matrix for mass ROI.

In addition as shown in **Figure 5**, a 9-D shape feature and a 7-D mass feature are extracted which representing the mass boundary and the average contrast, smoothness, orientation, uniformity, entropy, perimeter and circularity [17]. Finally, a 6-D texture feature representing the energy, correlation, entropy, inverse difference moment, contrast and homogeneity is obtained from the gray level co-occurrence matrix (GLCM).

5. Classification and similarity matching

For classification of breast masses as either normal and abnormal (two-class separation) or normal, benign, and malignant cases (three-class study), we used SVM and ELM classifiers for excellent generalization performance and little human intervention. The SVM carries out classification between two classes by determining a hyper plane in feature space that is based on the most informative points of the training set [47]. On the other hand, ELM is a single-hidden

layer feed-forward neural network (SLFNs) learning algorithm [48]. It first randomly assigns weights and biases for hidden nodes, and then analytically defines the output weights by using the least square method. Due to the random selection of weights and biases for hidden nodes, the ELM can decrease the learning time considerably and also can achieve superior generalization performance [49].

For similarity matching, it is challenging to find a unique feature representation to compare images accurately for all types of queries. Feature descriptors at different levels of image representation are in diverse forms and may be complementary in nature. The difference between the feature vector of queried mass (or ROI) and the feature vectors of reference images (or ROIs) is calculated to compute the similarity between the query image and the database. Current CAD schemes using CBIR approaches typically use the k-nearest neighbor type searching method which involves searching for the k most similar reference ROIs to the queried ROI. The smaller the difference ("distance"), the higher the computed "similarity" level is between the two compared ROIs. The searching and retrieving result of the CBIR algorithm depends on the effectiveness of the distance metrics to measure the "similarity" level among the selected images.

In this work, a fusion-based linear combination (Eq. (7)) scheme of similarity measure of different features is used with pre-determined weights. The similarity between a query image Iq and target image I_j is described as:

$$\mathrm{Sim}\left(I_q, I_j\right) = \sum_F \alpha^F S^F\left(I_q, I_j\right) = \sum_F \alpha^F S\left(f_q^F, f_j^F\right) \tag{7}$$

where $F \in \{NSCT, HOG, Shape, Mass, and GLCM\}$ and S^F (Iq, Ij) are the Euclidean similarity matching function in individual feature spaces and α^F are weights (determined experimentally) within the different image representation schemes.

6. Result evaluation

To evaluate the effectiveness of the proposed classification and retrieval-based decision support system, the experiments are performed on mammographic digitized images taken from the Digital Database for Screening Mammography (DDSM), a collaboratively maintained public dataset at the University of South Florida [23]. The DDSM database has been widely used as a benchmark for numerous articles on the mammographic area, for being free of charge and having a diverse quantity of cases. The database contains approximately 2500 cases where each case includes two image view anatomy (CC and MLO) of each breast (right and left). The size of the images varies from 1024 × 300 pixels to 1024 × 800 pixels. The DDSM database offers more than 9000 images and from where we selected a total of 5880 images for experiments and result evaluation.

6.1. Experiment design

To experiment with the classification systems, the entire collection of mammograms is divided where 40% of the images are chosen as the training set and the remaining 60% as the test set, and a 10-fold Cross Validation (CV) has been used in the experimental design. The SVM learning approach was examined with the Gaussian radial basis function (GRBF) (r = 2, C = 100). The

overall performance of a classifier is guaranteed by a 10-fold CV in all evaluation indices. The performance of ELM classifier depends on the selection of number of neurons in hidden layer L, which was determined as L = 700 by trials with increments within the range of 100–1000. It was found that both the training and testing errors were decreased when L increased to around 700 and after that the training and testing performance did not improve and kept almost fixed as shown in **Figure 6**. We also tested with different activation functions, such as sigmoid, tangent sigmoid, sin, and radial basis and the tangent-sigmoid found to be the optimal one.

6.2. Performance evaluation

For the performance evaluation of the proposed classification approaches in different feature spaces, we computed the sensitivity (true positive rate) and specificity (true negative rate) for each of the confusion matrices. The accuracy, sensitivity and specificity parameters are employed for the performance evaluation of our classification approaches. The specificity measures the percentage of positive instances that were predicted as positives, while sensitivity measures the percentage of negative instances that were predicted as negatives. The retrieval effectiveness is measured with the precision-recall (PR) graphs that are commonly used in the information retrieval domain. For the experiments, each image in the testing dataset is served as a query image. A retrieved image is considered to be a correct match if it belongs to the same category to which the query image belongs. The performances of the two image categories (e.g., normal and abnormal) and the three image categories (e.g., benign, malignant, normal) are compared, based on the PR graphs.

Finally, for both classification and retrieval evaluation, different combination of concatenated feature vectors are utilized as shown in **Table 1**. For example, the f_1 feature set consists of all five different features: Shape, Mass, GLCM, NSCT, eig(Hess)HOG features, whereas f_6 feature set consists of eig(Hess)HOG feature only.

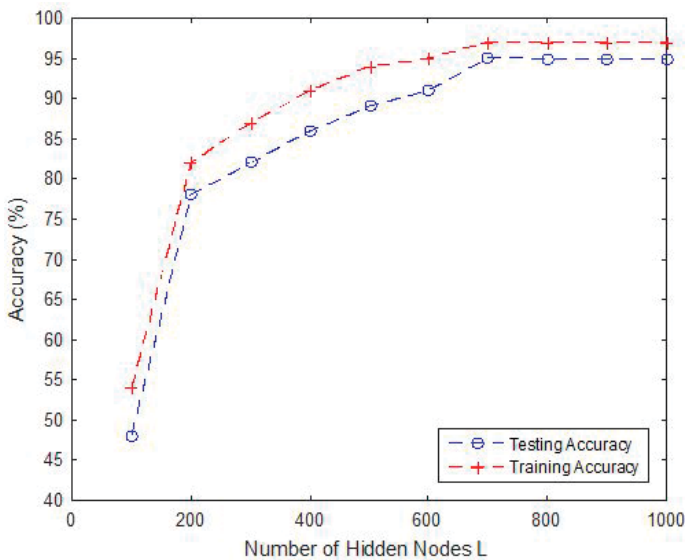

Figure 6. The number of hidden layer nodes L determination with L = 700.

6.3. Classification results

As mentioned, the classification accuracies in different feature sets of **Table 1** are compared and with both SVM and ELM classifier and it was found out that the f_1 feature set with ELM classifier is the most effective feature set in terms of accuracy, sensitivity, specificity both two and three class study. For example, **Tables 2** and **3** demonstrate the results for both 2- and 3- class studies for the f_1 and f_3 feature sets respectively.

From **Tables 2** and **3**, it can be observed that f_1 feature set is more effective than f_3 feature set in terms of accuracy, sensitivity, specificity both two and three class study. In fact, f_1 feature set with ELM as classifier achieved the highest classification accuracy rate in terms of mean accuracy, sensitivity and specificity parameters after 10-fold CV as shown in **Table 4**.

The classification efficiency, training and testing the performances of SVM and ELM were compared independently. As shown in **Table 4**, it can be seen that the proposed methods are effective on the DDSM database and ELM is a highly-effective classification technique

f	**Feature set**
f_1	Shape, Mass, GLCM, NSCT, eig(Hess)HOG
f_2	Shape, Mass, GLCM, NSCT
f_3	Shape, Mass, GLCM, eig(Hess)HOG
f_4	NSCT
f_5	NSCT, eig(Hess)HOG
f_6	eig(Hess)HOG

Table 1. Utilized different types of feature sets.

2 class				**3 class**		
Fold #	**Accuracy**	**Sensitivity**	**Specificity**	**Accuracy**	**Sensitivity**	**Specificity**
Fold 1	98.0167	96.5553	95.0939	86.1817	92.8298	92.7950
Fold 2	97.7035	95.8768	94.0501	94.1176	92.5861	93.5955
Fold 3	96.7641	95.5637	94.3633	93.5607	92.7602	92.5513
Fold 4	97.7035	95.9290	94.1545	93.1778	97.7035	98.9039
Fold 5	96.9729	94.6159	94.2589	97.7035	98.4342	98.0689
Fold 6	97.4948	95.9812	94.4676	98.7474	98.5386	98.6952
Fold 7	96.9729	95.8768	94.7808	98.5908	98.2255	91.3271
Fold 8	97.3904	96.2422	95.0939	92.6854	94.3574	95.7158
Fold 9	97.4948	97.0856	94.6764	94.1484	92.4765	92.8945
Fold 10	97.3904	95.6681	93.9457	93.4169	93.9394	93.8349
Ave	96.9729	95.5480	94.1232	92.4155	98.3612	93.4796

Table 2. Classification performance of f_1 feature set for the 2 and 3 class study.

2 class			3 class		
Fold #	**Accuracy**	**Sensitivity**	**Specificity**	**Accuracy**	**Sensitivity**	**Specificity**
Fold 1	95.0417	95.3549	95.0417	91.6464	89.7668	92.3773
Fold 2	94.7807	95.9812	95.1983	91.1939	91.3679	91.1939
Fold 3	95.2505	95.0939	94.9895	91.2287	92.5513	91.6812
Fold 4	95.4592	97.1816	96.2421	92.1685	98.8512	99.0078
Fold 5	95.9290	96.2421	97.7035	98.6945	99.3212	98.8512
Fold 6	96.2421	94.5720	96.7640	98.1723	98.4334	98.0157
Fold 7	98.3298	98.0167	92.9018	98.2768	99.1645	92.0668
Fold 8	94.4676	94.1544	93.3194	93.3194	92.6931	91.2317
Fold 9	94.2588	94.1544	95.9290	91.1274	92.0668	91.3361
Fold 10	93.4238	91.6492	92.9018	94.1545	94.1545	92.2756
Ave	95.2192	96.7223	93.7161	91.5176	98.6789	92.4426

Table 3. Classification performance of f_3 feature set for the 2 and 3 class study.

		Measures	f_1	f_2	f_3	f_4	f_5	f_6
2 class	ELM	Mean accuracy	96.973	95.709	95.219	93.742	92.228	94.665
		Mean sensitivity	95.548	97.223	96.722	96.743	97.421	99.853
		Mean specificity	94.123	94.196	93.716	90.741	87.035	89.478
	SVM	Mean accuracy	94.086	92.015	94.427	91.536	90.341	91.852
		Mean sensitivity	93.824	95.357	93.118	94.124	94.117	96.741
		Mean specificity	91.216	92.628	90.240	88.687	84.896	86.224
3 class	ELM	Mean accuracy	92.415	92.318	91.517	79.547	78.092	85.788
		Mean sensitivity	98.361	98.877	98.678	98.642	97.409	99.357
		Mean specificity	93.479	91.691	92.442	83.016	83.528	93.152
	SVM	Mean accuracy	90.125	89.654	89.884	76.004	74.011	83.256
		Mean sensitivity	95.244	94.519	95.331	94.875	92.546	95.446
		Mean specificity	89.886	87.359	90.214	79.954	80.820	89.744

Table 4. Performance comparisons of SVM and ELM classifiers using different features.

for this task. It is also proved to be highly efficient as lesser computational time was required compared to SVM with same sets but of different training data sizes.

Table 5 shows the comparison between our proposed system and a number of state-of-the-art classification systems. For the DDSM database, our classification system obtained comparable performance in accuracy, sensitivity and specificity. The promising results might be owing to the good segmentation algorithm as well as the effective feature extraction methods.

6.4. Retrieval results

A precision–recall curve based on our similarity fusion approach of different feature sets (f_1–f_6) is shown in **Figure 7**, which represents that f_1 feature set outperform the all other feature sets in terms of precision and recall. **Figure 8** shows that, when f_1 feature set are used, the cancer masses are the most discriminative among three types of masses.

The results verify that the characteristic of breast masses was better represented by the f_1 feature set, which was able to capture the difference between the gray level intensities of the breast densities. Concerning f_1 feature set, for a 4% of recall, a precision of 96% means that from 5880 mammogram images returned by the our proposed CBIR system, 5644 were relevant.

Literature	Database	Classifier	Accuracy (%)	Sensitivity	Specificity
Wang et al. [16]	DDSM	SVM	92.74	—	—
Liu and Tang [17]	DDSM	SVM	93.00	92.00	92.00
Dong et al. [18]	DDSM	GA-SVM	93.24	94.78	91.76
Jen and Yu [19]	DDSM	ADC	—	86.0	84.0
Wei et al. [30]	DDSM	ELM	95.73	—	—
Rouhi et al. [50]	DDSM	MLP	95.01	96.25	93.78
Jiao et al. [51]	DDSM	CNN	96.7	—	—
Proposed scheme	DDSM	ELM	96.973	95.548	94.123

Table 5. Classification performance of different methods.

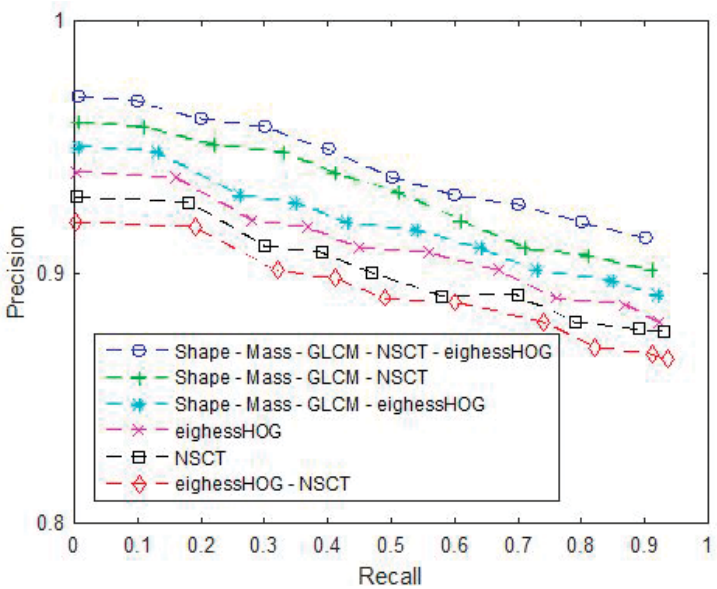

Figure 7. Performance evaluation of six feature sets on similar mass retrieval.

Figure 9 shows an example of a query image from benign category and retrieved images based on the f_1 feature set. The system retrieved all the top eight images from the same category of the query image and from the same direction (right). However, the views of top retrieved image are different where images 2, 3, 4 and 5 (left to right and top to bottom) are from MLO view while the others are from CC view. Another example of retrieval is demonstrated in

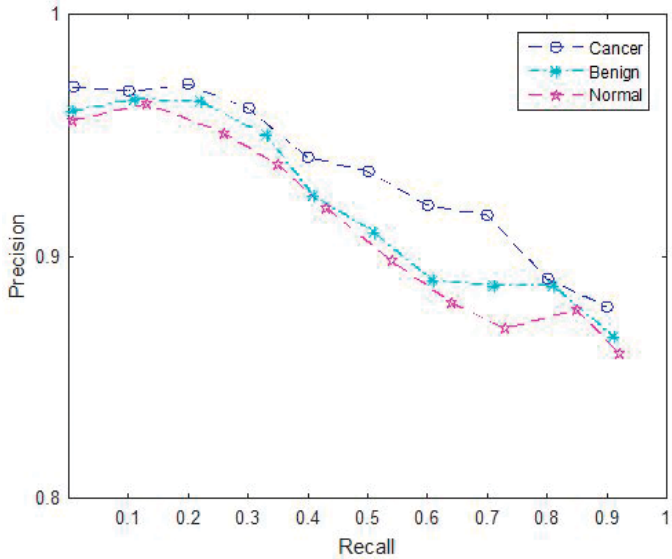

Figure 8. Performance evaluation of f_1 feature set on three different mass types of mass lesions.

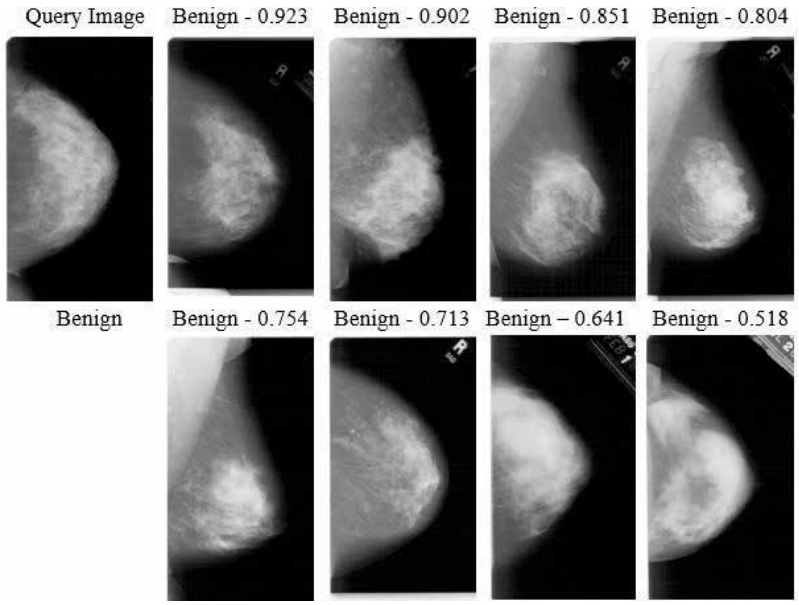

Figure 9. Retrieval example of one benign query of our proposed system using the f_1 feature set.

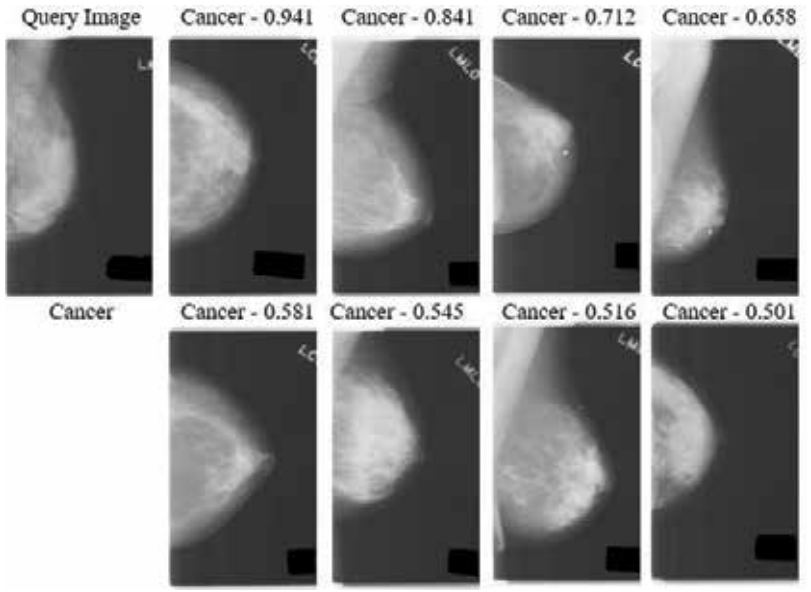

Figure 10. Retrieval example of one cancer query of our proposed system using the f_1 feature set.

Figure 10, using an image of cancer category. All the retrieved images are from the same category of the query image and from the same direction (right); however from both MLO (images, 2, 4, 7) and CC views. This might occur due to the fact that the ROI selected from these MLO images contains a good portion of pectoral muscle that was confused with the white part of the breast density.

The proposed system was implemented using the MATLAB through its image processing toolbox. Feature extraction and image retrieval were performed on an Intel i7 2.9 GHz processor with 8 GB of RAM under Microsoft Windows operating system.

7. Conclusions

In this paper, an integrated decision support system is proposed for the automated mass detection, classification and retrieval of mammograms. The system is evaluated for the retrieval and classification of the mammographic images. The experimental results indicate that the approach is effective to retrieve visually similar lesions from a database and to predict the categories of images for diagnostic correctness. The main objective of this paper is to demonstrate how the image retrieval and classification can be integrated and effectively utilized as a diagnostic support tool to help the radiologist for the mass detection. However, it is recognized that many other advanced image-based features and features from other sources would be necessary for a complete decision support system. In future, we plan to incorporate more advanced features related to the diagnostic relevance into our system and experiment with other classification and combination techniques as well. However, the presence of an

expert radiologist is still considered necessary for the overall visual assessment of the breast mass and the final diagnosis, based on the objective evaluation suggested by the system and contextual information from the patient data.

Author details

Mahmudur Rahman* and Nuh Alpaslan

*Address all correspondence to: md.rahman@morgan.edu

Department of Computer Science, Morgan State University, Baltimore, MD, USA

References

[1] Na. American Cancer Society published second edition of global cancer atlas. Oncology Times. 2015;**37**:34

[2] Al Mousa DS et al. Mammographic density and cancer detection. Academic Radiology. 2014;**21**:1377-1385

[3] Siegel RL, Miller KD, Jemal A. Cancer statistics, 2015. CA: A Cancer Journal for Clinicians. 2015;**65**:5-29

[4] Moura DC, Guevara López MA. An evaluation of image descriptors combined with clinical data for breast cancer diagnosis. International Journal of Computer Assisted Radiology and Surgery. 2013;**8**(4):561-574

[5] Jotwani A, Gralow J. Early detection of breast cancer. Molecular Diagnosis & Therapy. 2009;**13**(6):349-357

[6] Demircioğlu Ö, Uluer M, Arıbal E. How many of the biopsy decisions taken at inexperienced breast radiology units were correct? The Journal of Breast Health. 2017;**13**(1):23-26. DOI: 10.5152/tjbh.2016.2962

[7] Ganesan K, Acharya UR, Chua CK, Min LC, Abraham KT, Ng K-H. Computer-aided breast cancer detection using mammograms: A review. IEEE Reviews in Biomedical Engineering. 2013;**6**:77-98

[8] Rangayyan RM, Ayres FJ, Leo Desautels JE. A review of computer-aided diagnosis of breast cancer: Toward the detection of subtle signs. Journal of the Franklin Institute. 2007;**344**:312-348

[9] De Santo M, Molinara M, Tortorella F, Vento M. Automatic classification of clustered microcalcifications by a multiple expert system. Pattern Recognition. 2003;**36**:1467-1477

[10] Zhang Y, Tomuro N, Furst J, Raicu DS. Building an ensemble system for diagnosing masses in mammograms. International Journal of Computer Assisted Radiology and Surgery. 2011;**7**:323-329

[11] Buciu I, Gacsadi A. Directional features for automatic tumor classification of mammogram images. Biomedical Signal Processing and Control. 2011;**6**:370-378

[12] Tahmasbi A, Saki F, Shokouhi SB. Classification of benign and malignant masses based on Zernike moments. Computers in Biology and Medicine. 2011;**41**:726-735

[13] Tan M, Pu J, Zheng B. Reduction of false-positive recalls using a computerized mammographic image feature analysis scheme. Physics in Medicine and Biology. 2014; **59**:4357-4373

[14] Nascimento MZ, Martins AS, Neves LA, Ramos RP, Flores EL, Carrijo GA. Classification of masses in mammographic image using wavelet domain features and polynomial classifier. Expert Systems with Applications. 2013;**40**:6213-6221

[15] Nishikawa Robert M. Current status and future directions of computer-aided diagnosis in mammography. Computerized Medical Imaging and Graphics. 2007;**31**(4-5):224-235

[16] Wang Y, Li J, Gao X. Latent feature mining of spatial and marginal characteristics for mammographic mass classification. Neurocomputing. 2014;**144**:107-118

[17] Liu X, Tang J. Mass classification in mammograms using selected geometry and texture features, and a new SVM-based feature selection method. IEEE Systems Journal. 2014;**8**:910-920

[18] Dong M, Lu X, Ma Y, Guo Y, Ma Y, Wang K. An efficient approach for automated mass segmentation and classification in mammograms. Journal of Digital Imaging. 2015;**28**:613-625

[19] Jen C-C, Yu S-S. Automatic detection of abnormal mammograms in mammographic images. Expert Systems with Applications. 2015;**42**:3048-3055

[20] Zheng B. Computer-aided diagnosis in mammography using content-based imageretrieval approaches: Current status and future perspectives. Algorithms. 2009;**2**(2):828-849

[21] Alto H, Rangayyan RM, Desautels JEL. Content-based retrieval and analysis of mammographic masses. Journal of Electronic Imaging. 2005;**14**(2):023016

[22] Kinoshita SK, de Azevedo-Marques PM, Pereira RR, Rodrigues JAH, Rangayyan RM. Content-based retrieval of mammograms using visual features related to breast density patterns. Journal of Digital Imaging. 2007;**20**(2):172-190

[23] Tie L et al. Learning to detect a salient object. IEEE Transactions on Pattern Analysis and Machine Intelligence. 2011;**33**:353-367

[24] Da Cunha AL, Zhou J, Do MN. The nonsubsampled Contourlet transform: Theory, design, and applications. IEEE Transactions on Image Processing. 2006;**15**:3089-3101

[25] Hanbay K, Alpaslan N, Talu MF, Hanbay D, Karci A, Kocamaz AF. Continuous rotation invariant features for gradient-based texture classification. Computer Vision and Image Understanding. 2015;**132**:87-101

[26] Heath M. et al. Current Status of the Digital Database for Screening Mammography. In: Karssemeijer N, Thijssen M, Hendriks J, van Erning L, editors. Digital Mammography. vol 13. Dordrecht: Computational Imaging and Vision, Springer; 1998

[27] Wang XH et al. Automated assessment of the composition of breast tissue revealed on tissue-thickness-corrected mammography. American Journal of Roentgenology. 2003;**180**:257-262

[28] Muramatsu C et al. Determination of subjective similarity for pairs of masses and pairs of clustered microcalcifications on mammograms: Comparison of similarity ranking scores and absolute similarity ratings. Medical Physics. 2007;**34**:2890

[29] de Oliveira JEE, Machado AMC, Chavez GC, Lopes APB, Deserno TM, Araújo AA. MammoSys: A content-based image retrieval system using breast density patterns. Computer Methods and Programs in Biomedicine. 2010;**99**:289-297

[30] Wei L, Yang Y, Nishikawa RM. Microcalcification classification assisted by content-based image retrieval for breast cancer diagnosis. Pattern Recognition. 2009;**42**:1126-1132

[31] Wei C-H, Li Y, Huang PJ. Mammogram retrieval through machine learning within BI-RADS standards. Journal of Biomedical Informatics. 2011;**44**:607-614

[32] Brake GM, Karssemeijer N. Segmentation of suspicious densities in digital mammograms. Medical Physics. 2001;**28**:259-266

[33] Zheng B, Chang YH, Gur D. Computerized detection of masses in digitized mammograms using single image segmentation and multi-layer topographic feature extraction. Academic Radiology. 1995;**2**:959-966

[34] Lobregt S, Viergever MA. A discrete dynamic contour model. IEEE Transactions on Medical Imaging. 1995;**14**:12-24

[35] Yuan Y, Giger ML, Li H, Suzuki K, Sennett C. A dual-stage method for lesion segmentation on digital mammograms. Medical Physics. **34**:4180-4193

[36] Dominguez AR, Nandi AK. Improved dynamic-programming-based algorithms for segmentation of masses in mammograms. Medical Physics. 2007;**34**:4265-4268

[37] Agrawal P, Vatsa M, Singh R. Saliency based mass detection from screening mammograms. Signal Processing. 2014;**99**:29-47

[38] Avraham T, Lindenbaum M. Esaliency (extended saliency): Meaningful attention using stochastic image modeling. IEEE Transactions on Pattern Analysis and Machine Intelligence. 2010;**32**(4):693-708

[39] Meselhy Eltoukhy M, Faye I, Belhaouari Samir B. A comparison of wavelet and curvelet for breast cancer diagnosis in digital mammogram. Computers in Biology and Medicine. 2010;**40**:384-391

[40] Ergin S, Kilinc O. A new feature extraction framework based on wavelets for breast cancer diagnosis. Computers in Biology and Medicine. 2014;**51**:171-182

[41] Choi JY, Ro YM. Multiresolution local binary pattern texture analysis combined with variable selection for application to false-positive reduction in computer-aided detection of breast masses on mammograms. Physics in Medicine and Biology. 2012;**57**:7029-7052

[42] Lahmiri S, Boukadoum M. Hybrid discrete wavelet transform and Gabor filter banks processing for features extraction from biomedical images. Journal of Medical Engineering. 2013;**2013**:1-13

[43] Reyad YA, Berbar MA, Hussain M. Comparison of statistical, LBP, and multi-resolution analysis features for breast mass classification. Journal of Medical Systems. 2014;**38**(9):100. DOI: 10.1007/s10916-014-0100-7. [Epub 2014 Jul 19]

[44] Shah VP, Younan NH, King RL. An efficient pan-sharpening method via a combined adaptive PCA approach and Contourlets. IEEE Transactions on Geoscience and Remote Sensing. 2008;**46**:1323-1335

[45] Do MN, Vetterli M. The contourlet transform: An efficient directional multiresolution image representation. IEEE Transactions on Image Processing. Dec. 2004;**14**:2091-2106

[46] Dalal N, Triggs B. Histograms of Oriented Gradients for Human Detection. In: 2005 IEEE Computer Society Conference on Computer Vision and Pattern Recognition (CVPR'05), San Diego, CA, USA; 2005;**1**:886-893. DOI: 10.1109/CVPR.2005.177

[47] Burges JC. A tutorial on support vector machines for pattern recognition. Data Mining and Knowledge Discovery. 1998;**2**:121-167

[48] Huang GB, Zhu QY, Siew CK. Extreme learning machine: Theory and applications. Neurocomputing. 2006;**70**:489-501

[49] Xie W, Li Y, Ma Y. Breast mass classification in digital mammography based on extreme learning machine. Neurocomputing. 2016;**173**:930-941

[50] Rouhi R, Jafari M, Kasaei S, Keshavarzian P. Benign and malignant breast tumors classification based on region growing and CNN segmentation. Expert Systems with Applications. 2015;**42**:990-1002

[51] Jiao Z, Gao X, Wang Y, Li J. A deep feature based framework for breast masses classification. Neurocomputing. 2016;**197**:221-231

Chapter 3

Medical Imaging and Image-Guided Interventions

Abdelmoneim Sulieman and
Mohammed Alkhorayef

Additional information is available at the end of the chapter

http://dx.doi.org/10.5772/intechopen.76608

Abstract

The discovery of X-rays at the end of the nineteenth century is one of the most important discoveries that changed the human being life in all fields and applications. Since that date, X-ray systems are developed rapidly, and still new applications are emerging in medical, agricultural, and industrial fields. This chapter provides sufficient historical background for X-ray production and image acquisition techniques. It covers also fluoroscopic equipment and radiation dosimetry and protection techniques in detail. Image-guided intervention is here to stay. Thus, suitable radiation protection measures are required to minimize the risk to patients and staff to its minimal level without affecting the outcome of the procedures.

Keywords: medical imaging, X-ray, radiation risk, radiobiological effect, skin injury, interventional radiology

1. Background

Since the discovery of X-rays accidentally by Professor Wilhelm Roentgen (from March 27, 1845 to February 10, 1923), a German scientist, Rector of Wurzburg University on Friday, November 8, 1895, a huge development was occurred in the technology of X-ray machines and its applications [1]. He provisionally called these as X-rays. Afterward, he and other scientists performed systemic scientific research to define the newly discovered X-rays. Few months later, in February 1896, in recognition of his discovery, the scientific community named these X-rays as Roentgen rays [2]. Later in 1901, Roentgen awarded the first Nobel Prize in Physics in recognition of his discovery. Recently in 2004, the International Union of Pure and Applied Chemistry, in honor of Roentgen, named the highly radioactive element with atomic number 111 Roentgenium ($^{280}Rg_{111}$) (**Figure 1**) [6].

Figure 1. William Roentgen.

Figure 2. The first X-ray image (left hand of Bertha Roentgen).

The first X-ray image of a human was the hand of Wilhelm Roentgen's wife Bertha Roentgen on December 22, 1895. This opened the door for medical applications of X-rays (**Figure 2**). At that time, X-rays were only known as a form of electromagnetic radiation (photons) with short wavelength ranged from 10^{-2} to 10^{-9} nanometer.

2. Characteristics of X-rays

Other main characteristics were revealed including:

1. Penetration: X-rays can penetrate most objects, and the penetration ability depends on photon energy (tube voltage (kVp)) and the object medium characteristics (thickness, density and the atomic number). The X-ray penetration ability is inversely dependent on medium characteristics.
2. Ionization and excitation of atoms: X-rays have sufficient energy to ionize air, i.e., eject electron from an atom, producing positive ion and free electron. As hydrogen is the atom with a minimal binding energy (−13.5 eV), which considered the threshold energy between ionizing and nonionizing radiation, photons of energy higher than 13.5 eV are ionizing radiation. Excitation occurs when the orbital electron absorbed energy less that its binding energy, which resulted in raising electrons to higher energy levels. Ionization of gas is the oldest method of radiation detection and dosimetry.
3. Fluorescence: X-rays can cause certain materials such as calcium tungstate to emit visible light. This is one of the major characteristics of X-rays used in medical imaging, which resulted in reduction of patient radiation dose by using intensifying screens and conversion of X-rays to visible light. Fluoroscopy is used to obtain dynamic images for diagnostic and/or therapeutic purposes.
4. Photographic effect: X-rays can produce a silver ion (Ag^+) and an electron when they interact with silver bromide (AgBr) or silver iodide (AgI) (photosensitive materials which are sensitive to X-rays and light). This effect is invisible (latent imaging) and can be converted to visible image via development or processing. X-rays have different shades of gray based on the X-ray beam absorption in the body. The conventional X-ray film consists of 98% AgBr and 2% AgI.
5. Chemical effect: X-rays can produce chemical alterations in certain materials. This chemical change in living organism can lead to biological effect (see list 7). The accurate quantification of the chemical change in the absorbing material enabled scientists to measure the absolute radiation dose (Fricke dosimeter).
6. Thermal effects: when a medium is exposed to X-rays, tiny amount of energy is converted to heat, and thus increases the medium temperature. If a suitable calorimeter is used, the absolute absorbed dose can be estimated in relation to medium temperature.
7. Biological effect: One of the major effects of radiation is the ability to cause damage to cells, organs, or organisms. Thus, patients, staff, and public protection are major concerns in medical imaging. On the other hand, these biological effects are used to destroy cancerous cells and cure patients with fatal diseases.

8. Medical imaging: radiographic imaging is used to extract patients' anatomical and physiological data in order to diagnose a clinical condition. Image formation consists of the following stages:
    1. X-ray passes through the patient during imaging procedures.
    2. As X-rays penetrate through the body tissues, it become modified and each part of the beam is attenuated in a degree that depends on:
        a. the tissue type;
        b. the intensity of the beam; and
        c. thickness of the tissue.
    3. A suitable image receptor receives the signal and creates radiograph with different levels of gray scales according to the tissue attenuation.

3. Image-guided interventions

Interventional radiology is a newly emerged branch from radiology using fluoroscopic guidance to perform complex procedure noninvasively. Nowadays, many imaging modalities are used in the field of image-guided interventions. These imaging technologies include, in addition to planar fluoroscopy, CT, MRI, and ultrasound. The image-guided intervention techniques expanded rapidly due to its numerous advantages including local anesthesia and low rate of mortality and morbidity (short stay at hospital).

3.1. Fluoroscopy

Fluoroscopy, or real-time imaging, is an imaging technique that produces dynamic images at low tube current range from 0.5 to 5.0 mA for longtime intervals, resulting in dynamic images with lesser image quality. The fluoroscopy played a fundamental role in emergence of interventional radiology since its introduction by Thomas Edison (1847–1931) in May, 1896, just an year after the discovery of X-rays. The early fluoroscope composed of fluorescent screen (zinc-cadmium sulfide) placed over the patient's body between the patient and radiologist (**Figure 3**) at complete darkness, and the radiologist looked directly at the screen. Dark adaptation was required from 10 to 30 minutes by wearing red goggles to enhance viewing.

3.2. Contrast medium

From the early days of medical application of X-rays, practitioners noticed the need of soft tissue and blood vessels imaging. Thus, many experiments were conducted in order to alter the absorption characteristic (atomic number) of the tissue in relation to their adjacent structures (soft tissue effective atomic number ≈ 7.4). Thus, negative contrast media (air) and positive contrast media were developed for gastrointestinal tract in 1910, for oral and rectal administration

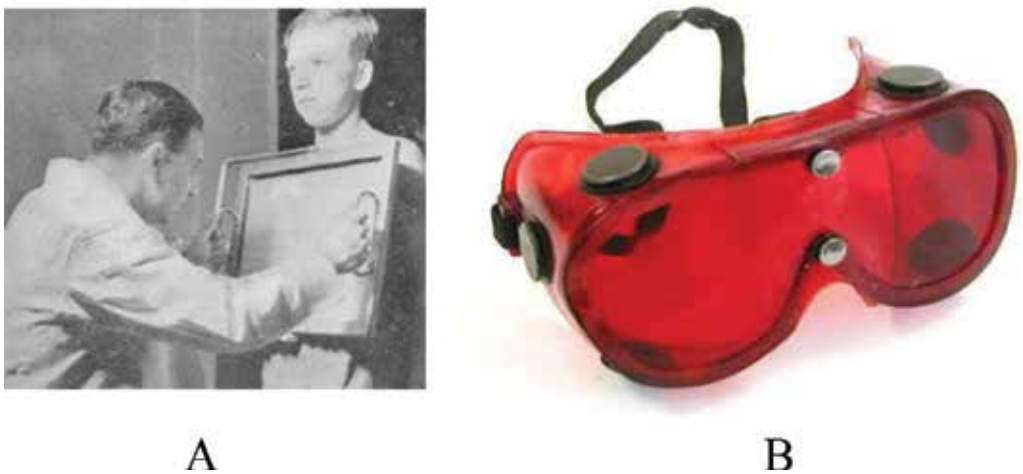

Figure 3. (A) Radiologist using a fluoroscope during an examination; and (B) red goggles.

exclusively (barium sulfate ($BaSO_4$), with effective atomic number 56), and gastrografin (Diatrizoate Meglumine and Diatrizoate Sodium Solution, effective atomic number 53), which is an iodinated soluble contrast medium, was developed in 1954. For cardiovascular system, urografin (amidotrizoate meglumine; sodium amidotrizoate ($C_{11}H_9I_3N_2O_4$)) was developed [2].

Afterward, the clinical experiments on cardiac catheterization and angiography progressed extensively, and in 1956, Forssman and Cournand received the Nobel Prize in physiology and medicine for their efforts in development of cardiac catheterization [3].

The image-guided intervention was started as a diagnostic technique, but due to the development of recent imaging technology such as CT angiography and magnetic resonance angiography (MRA), it becomes a pure therapeutic technique. Image-guided intervention is performed usually under fluoroscopic guidance. However due to the development of other imaging modalities such as CT, MRI, and ultrasound, these techniques are progressing with some drawbacks that include radiation risk in CT imaging, metallic surgical tools as a limitation for MRI application in interventional procedures, and ultrasound poor image quality [4]. In addition to that, a combination of fluoroscopy with endoscopy provided also excellent approach to treat many clinical conditions.

4. Image-guided intervention instrumentation

Fluoroscopic equipment was developed in 1896 by Thomas Edison. At that time, very simple instruments were used without any consideration of radiation protection for patients and staff (**Figure 3B**). Since that date, fluoroscopy equipment technology developed rapidly, and new applications are emerging continuously (**Figure 3A**; old practice in fluoroscopy).

4.1. Types of fluoroscopic equipment

Fluoroscopic equipment is classified into two types:

4.1.1. General purpose fluoroscopy X-ray machine

The first type is a general purpose fluoroscopy X-ray machine (permanently fixed fluoroscopic unit) which is usually installed at radiology departments or other interventional radiology departments such as orthopedic. There are two configurations of permanent units: fluoroscopic unit with under couch X-ray tube and over couch image intensifier or vice versa. Over couch X-ray unit has some advantages including better flexibility in patient positioning, possibility to use the same X-ray tube for radiography imaging with stand Bucky, and possibility to adjust source-skin distance. However, over couch X-ray units are not recommended for interventional procedures because staff exposure increases five to six times compared with under couch X-ray tube and over couch image intensifier configuration [5]. The minimum source (X-ray tube) to skin distance must be at least 30.5 cm away from the surface of skin. Modern C arm machine has mobile spacer cones to maintain the correct distance. Operator can remove the cone temporarily if it interferes with the procedure in under couch position. The other configuration is C arm unit. C arm is an X-ray unit where the image intensifier (flat-panel detector (FPD)) and X-ray tube are at two ends of the letter C as illustrated in **Figures 4** and **5**. C arm equipped with FPD, which costs three times, has the capability to produce better image quality compared with image intensifier. C arm is utilized to provide more wherever greater flexibility in image acquisition at different projections (views). The machine is used to perform minimally invasive procedures such as cardiac catheterization, angiography, orthopedic, gastroenterology and therapeutic interventional procedures. Recent development in imaging technology enables C arm system to obtain fluoroscopy images and 3D cone-beam CT (CBCT) images. Vascular studies are usually performed in fixed fluoroscopy unit. A C-arm X-ray machine is preferable because it can be rotated rather than the patient during the procedure. Some fluoroscopic X-ray systems are equipped with two radiation sources, which enable reduction of the number of injections of contrast required.

Figure 4. Modern C arm X-ray machine (large).

Figure 5. Mini C arm X-ray machine used for pediatric and extremities (1/10th of large C arm dose).

4.1.2. Mobile C arm

The second type is mobile C arm, which is more convenient and can be moved from one place to another according to the need of the operator, and image can be transferred via Bluetooth in modern equipment to the printer. Thus, C arm is commonly used in operation rooms.

C arm has two types:

a. large C arm; and

b. mini C arm.

Mini C arms are small fluoroscopes used mainly in orthopedic procedures (extremities) and pediatric procedures. Operators can control the fluoroscopic unit from the control panel and inside the room with a foot pedal. The image quality is lower in fluoroscopy compared with radiography due to low tube current used in the first one. The dose is lowered by 45–60% during fluoroscopy image acquisition compared with radiography [6]. Auto fluoroscopy is an option that provides an optimum tube current (mA) to provide sufficient image quality. Acceding to the international recommendations, pulsed fluoroscopy intermittent pulses (from 2 to 30 times per second) are used to reduce patient doses during the procedures by 50% of its initial value while maintaining image quality. Digital fluoroscopic units are capable to store images from the detector (fluorography) and last image hold (the last frame acquired is left on the monitor after the X-ray beam is switched off).

5. CT fluoroscopy (CTF)

The substantial advances in CT technology have led to development in CT fluoroscopy in 1993, which allows fluoroscopic image acquisition with high image quality compared to conventional fluoroscopy [7]. This development in CT technology (slip ring technology in 1980s and X-ray tubes with high anode heat storage capacity up to 30 million heat units (MHU) or 22,000 kJ) and high speed processing units and advances in reconstruction software, enabled acquisition of high image quality in a short time with lower radiation dose) [8]. CT fluoroscopy becomes popular in image-guided intervention despite of the concern regarding radiation risks due to its advantages compared with conventional fluoroscopy and surgery. CT fluoroscopy is very valuable biopsy for deep structures, stent placement, and lesion drainage. CT fluoroscopy is usually performed using the following exposure parameters: 120 kVp, 30–90 mA, scan time range from 0.5 to 1.0 s, and fluoroscopic images displayed in certain time interval range between 3 s^{-1} and `12 s^{-1} [9].

6. Radiation doses from image-guided intervention procedure

Fluoroscopy screening exposure time during image-guided intervention depends upon the type of the procedure and operator skills and X-ray machine technology and machine set up. Different procedures have different screening times. Usually, cardiology intervention procedure requires longer screening time compared with orthopedic procedures.

6.1. Tissue reaction during interventional procedure

When X-ray radiation penetrates a tissue or a medium, it deposits energy. The energy absorbed from exposure to radiation is termed a dose. Certain interventional procedure requires prolonged exposure time. These procedures are:

a. Vascular embolization

b. Stent and filter placement

c. Thrombolytic and fibrinolytic procedures

d. Percutaneous transhepatic cholangiography

e. Radio-frequency cardiac catheter ablation

f. Percutaneous transluminal angioplasty (coronary and other vessels)

g. Endoscopic retrograde cholangiopancreatography

h. Transjugular intrahepatic portosystemic shunt placement

i. Percutaneous nephrostomy

j. Biliary drainage or urinary or biliary stone removal

6.2. Tissue reaction in image-guided intervention

The dose rate during fluoroscopic-guided intervention ranged between 0.02 and 0.05 Gy/minute [10]. It was estimated that the mean patient dose for cardiac catheterization is 2.5 Gy, and during percutaneous interventions, the dose may reach 6.4 Gy per procedures, which is higher than the erythema dose [11]. Erythema occurs due to accumulative patient doses from multiple procedures, each of which is individually insufficient to cause injury. Most of the patients require more than one procedure within a short time such as patients with ischemic heart diseases (IHD). **Table 1** shows the tissue reaction threshold during image-guided intervention procedures using fluoroscopy. **Table 2** illustrates the biological effect on patients after exposure to certain doses. **Figures 6–11** show radiation-induced skin injuries due to prolonged irradiation.

Deterministic effect	Typical threshold dose (Gy)*	Time of onset*
Early transient erythema	2	~2–24 hours
Temporary epilation	3	~3 weeks
Main erythema	6	~10 days
Permanent epilation	7	~3 weeks
Invasive fibrosis	10	—
Dry desquamation	14	~4 weeks
Late erythema	15	~8–10 weeks
Moist desquamation	18	~4 weeks
Ischemic dermal necrosis	18	>10 weeks
Secondary ulceration	24	> 6 weeks
Dermal atrophy (1st phase)	10	>52 weeks
Telangiectasia	10	> 52 weeks
Dermal necrosis (delayed)	>12	>52 weeks

*actual skin dose not entrance surface air kerma

Table 1. Tissue reaction effects of acute radiation exposure.

Radiation equivalent dose (Sv)	Subsequent effect
0.25	Blood changes (e.g., measurable hematologic depression, decrease in the number of lymphocytes present in the circulating blood)
1.5	Nausea, diarrhea
2.0	Erythema (diffuse redness over an area of skin after irradiation)
2.5	If dose is administered to gonads, temporary sterility
3.0	50% chance of death
6.0	Death

Table 2. Biological effects of radiation [11, 12].

Figure 6. Tissue reaction effect for a 49-year-old patient who underwent two transjugular intrahepatic portosystemic shunt (TIPS) placements and one attempted TIPS placement within a week [12].

Figure 7. Photograph of right posterolateral chest wall at 10 weeks after PTCA for a 56-year-old man with obstructing lesion of right coronary artery [12].

http://dx.doi.org/10.5772/intechopen.76608

Figure 8. Secondary ulceration after two months for a 69-year-old patient underwent two angioplasties of left coronary artery within 30 hr [12].

Figure 9. Skin telangiectasia after 2 years for a 17-year-old patient underwent two cardiac ablations procedures within 13 month [12].

Figure 10. Radiation wound 22 months after angioplasty procedure [15].

Figure 11. Radiation injury in a 60-year-old woman subsequent to successful neurointerventional procedure for the treatment of acute stroke [11].

7. Patient doses measurement

When performing radiographic examinations, patient doses can be evaluated as entrance surface air kerma (ESAK), the dose administered to the skin, where an X-ray beam enters the body, which includes the incident air kerma and backscattered radiation from exposed tissue. ESAK is measured using dosimeters or through calculations from the applied exposure factors and measurements of X-ray tube output [13]. Another method is the kerma-area product (KAP), defined as the product of the dose in air (air kerma) within the X-ray beam and the beam area, which enables the measurement of overall radiation entering a patient. KAP can be measured using an ionization chamber fitted to the X-ray tube. The two methods can be applied to calculate and monitor radiation doses for the various radiological examinations compared to guidance and diagnostic reference levels (DRLs). Many research bodies have been active in the area of DRL, including the International Atomic Energy Authority (IAEA) and International Commission on Radiological Protection (ICRP). The objective of DRLs is to aid in preventing the administration of unnecessary radiation doses to patients that do not support the clinical purpose of a radiographic exam. Each X-ray facility should set up DRLs following international guidelines with regular assessments and applications of corrective action in cases where these levels are exceeded.

8. Quality assurance

Quality assurance in medical imaging intends to ensure the consistent provision of prompt and accurate diagnosis of patients with minimum radiation exposure to patient and staff and to be cost-effective.

8.1. Image quality

Image quality, which is defined as the exactness of representation of patient anatomy, is affected by many factors including organ of interest, imaging modality, patient, and imaging modality characteristics. Images in clinical environment are evaluated subjectively by operators (radiography technologist or radiologists) or objectively (independently of an observer opinion) by measuring certain parameters. These parameters include brightness, contrast resolution, special resolution distortion, artifact, and noise, as illustrated in **Table 3**.

Tables 4 and **5** show factors affecting patient doses during interventional procedures. Patient dose depends, among other factors, on X-ray unit technology, proper equipment design and utilization, proper set up of equipment parameters, and operator skills.

Optimization in diagnostic radiology signifies balancing diagnostic information (image quality) and patient dosage through identifying an image acquisition technique that maximizes the perceived information content and minimizes radiation risk or keeps it at a reasonably low level (ALARA).

The factors that affect patient dose and image quality and form the backbone of optimization in diagnostic radiology fall into three categories: facilities and equipment, operational conditions, and application factors.

Image quality factor	Definition/controlling factor(s)
Brightness	• **Definition:** the intensity of light representing image pixels on the monitor • **Controlling factors:** the optimal digital image brightness is influenced by a wide range of exposure factors and controlled by processing software through digital processing algorithms. The operator can apply post processing algorithms to modify pixel values of the image. Windowing is used to manipulate and adjust the brightness of the digital image after exposure by altering the window level (WL) within a certain range. Smoothing and edge enhancement of the image can also be increased for better brightness.
Contrast	• **Definition:** the difference in brightness between light and dark areas of an image • **Controlling factors:** control of scatter radiation is an important factor in obtaining the appropriate image contrast through correct use of grid, close collimation, and selection of optimal kVp • Radiographic contrast is affected by the digital processing computer through application of predetermined algorithms. Through post processing, the user can manipulate the contrast of the digital image
Resolution	• **Definition:** the recorded sharpness or detail of structures on the image • **Controlling factors:** traditional factors as for film screen imaging besides acquisition pixel size inherent to the digital imaging detector and display matrix. Perceived resolution of the image dependent on the display capabilities of the monitor
Distortion	• **Definition:** the misrepresentation of an object size or shape as projected onto recording media • **Controlling factors:** as for film screen imaging, the factors that affect distortion are the source image receptor distance (SID), object image receptor distance (OID), object image receptor alignment, and central ray alignment (**Table 1**)
Artifact	• **Definition:** EI is a measure of the amount of exposure received by the image receptor • **Controlling factors:** EI is dependent on mAs, total detector area irradiated, and beam attenuation. The exposure index is indicative of image quality. Equipment manufacturers provide a recommended EI range for optimal image quality
Noise	• **Definition:** random disturbance that obscures or reduces clarity. • **Controlling factors:** technologists must ensure that exposure factors used for examination are not beyond those required for the projection by checking the exposure index to avoid needless overexposure of the patient. On the other hand, scattered radiation is a potential source of noise that can be controlled by the use of grids and correct collimation. Image noise may also be related to the electronic system, nonuniformity of the image receptor, or power fluctuations. • Increasing input doses • Frame averaging—smooth by adding successive images at the expense of temporal resolution

Table 3. Image quality factors and their controlling/influencing factors in DR.

8.2. Establishment of diagnostic reference levels

To improve the optimization in diagnostic procedures, the ICRP recommends the use of diagnostic reference levels (DRLs) to ensure that the doses do not deviate significantly from internationally reported levels to those achieved at peer departments for that procedure unless

Parameter	Control of parameter	Management
Patient size	Not controllable	Increase the exposure parameters
Type of procedure and pathology	Not controllable	Therapeutic procedures require more fluoroscopic time than diagnostic procedures
Patient setup	Controllable	Accurate patient positioning before the procedure reduces the need for patient positing using fluoroscopy
Patient preparation and communication	Controllable	Good patient communication increases patient cooperation and reduces the possibility of patient movement during the exposure and hence minimizes the possibility of image blurring

Table 4. Patient related factors affecting patient radiation doses.

Parameter	Control of parameter	Management
Experience	Not controllable	Increase the exposure parameters
Radiation dose monitoring	Not controllable	Therapeutic procedures require more fluoroscopic time than diagnostic procedures
Dose reference levels	Controllable	DRL could be used to improve patient dose management in order to avoid unnecessary radiation exposure
Use of specified protocol	Controllable	Good patient communication increases patient cooperation and reduces the possibility of patient movement during the exposure and hence minimizes the possibility of image blurring
Collimation	Controllable	Proper collimation of radiation to the region of interest reduces patient and staff dose and improves image quality
Radiographic images	Controllable	The number of image is proportional to patient dose
Fluoroscopy time	Partially controllable	Fluoroscopy time is proportional to dose
Magnification	Controllable	Radiation dose in increasing by magnification
Dose mode	Controllable	Low dose mode setting requires low tube current and less patient dose
Image geometry	Controllable	Increasing the source-skin distance (SSD) and decreasing patient detector distance reduces patient doses

Table 5. Operator related factors affecting patient radiation doses.

there is a known, relevant, and acceptable reason for this deviation. Practitioners and referrers should understand the following hits about DRLs for best practices [14]:

1. DRLs are not dose limits; they should be used as investigation levels;
2. DRLs are not applicable to individual patients;
3. comparison with DRLs shall be made using mean/median values of a sample of patient doses;
4. the use of DRLs should be made in conjunction with the evaluation of the required image quality or diagnostic information;

5. DRLs should be applied with flexibility, allowing tolerances for patient size, condition, etc.;
6. values that are UNDER the DRLs may not necessarily be optimized values;
7. values that are OVER the DRLs should require an investigation and optimization of the X-ray system or operational protocols;
8. the goal in using DRLs is not to reduce patient doses if image quality or diagnostic information is compromised; and
9. compliance or faults with DRLs should be discussed with the staff of the imaging department.

9. Conclusions

Image-guided intervention is safe and effective technique of choice to replace invasive intervention such as surgery. The frequency of interventional procedures is increasing and expected to increase in the future. Advances in imaging modalities will lead to introduction of a new complex interventional procedure. The risks of radiation-induced skin injuries (erythema) are expected in all complex procedures. Training of staff in fluoroscopic techniques will prevent patients from avoidable radiation risks and skin injuries.

Author details

Abdelmoneim Sulieman[1,2]* and Mohammed Alkhorayef[3,4]

*Address all correspondence to: abdelmoneim_a@yahoo.com and a.sulieman@psau.edu.sa

1 Department of Radiology and Medical Imaging, College of Applied Medical Sciences, Prince Sattam Bin Abdulaziz University, Al-Kharj, Saudi Arabia

2 Basic Science Department, College of Medical Radiologic Sciences, Sudan University of Science and Technology, Khartoum, Sudan

3 Department of Radiological Sciences, College of Applied Medical Sciences, King Saud University, Riyadh, Saudi Arabia

4 Centre for Nuclear and Radiation Physics, Department of Physics, University of Surrey, Guildford, Surrey, UK

References

[1] Glasser O. Wilhelm Conrad Röntgen and the Early History of the Roentgen Rays

[2] Thomsen H, Muller RN, Mattrey RF. Trends in Contrast Media. Springer Science & Business Media; 2012. p. 13

[3] Bruschke AV, Sheldon WC, Shirey EK, Proudfit WL. A half century of selective coronary arteriography. Journal of the American College of Cardiology. 2009;**54**(23):2139-2144

[4] Bowsher WG, Blott P, Whitfield HN. Radiation protection in percutaneous renal surgery. British Journal of Urology. 1992;**69**:231-233

[5] Sulieman A, Theodorou K, Vlychou M, Topaltzikis T, Kanavou D, Fezoulidis I, et al. Radiation dose measurement and risk estimation for paediatric patients undergoing micturating cystourethrography. The British Journal of Radiology. 2007;**80**:731-737

[6] Periodic Table. Royal Society of Chemistry. Available at: http://www.rsc.org/periodic-table/element/111/roentgenium [Accessed: January 18, 2018]

[7] Froelich JJ1, Wagner HJ. CT-fluoroscopy: Tool or gimmick? Cardiovascular and Interventional Radiology. 2001;**24**(5):297-305

[8] Siemens Medical Computed Tomography (CT) Scanners. Available at: https://www.oncologysystems.com/diagnostic-imaging/ct-scanners/siemens-med.php [Accessed: January 29, 2018]

[9] Keat N. Real-time CT and CT fluoroscopy. British Journal of Radiology. 2001;**74**:1088-1090

[10] Goldman LW. Principles of CT and CT Technology. Journal of Nuclear Medicine Technology. 2007;**35**:115-128

[11] Balter S, Hopewell JW, Miller DL, Wagner LK, Zelefsky MJ. Fluoroscopically guided interventional procedures: A review of radiation effects on patients' skin and hair. Radiology. 2010;**54**(2):326-341

[12] Granel F, Barbaud A, Gillet-Terver MN, et al. Radiodermites chroniques après cathétérisme interventionnel cardiaque: Quatre observations. Ann Dermatol Venereol 1998;**125**:405-407

[13] George J, Eatough JP, Mountford PJ, et al. Patient dose optimization in plain radiography based on standard exposure factors. The British Journal of Radiology. 2004; **77**(922):858-863

[14] IAEA: Human Health Campus. Computed radiography and digital radiography. Available at http://nucleus.iaea.org/HHW/MedicalPhysics/DiagnosticRadiology/PerformanceTesting/Computedradiographyanddigitalradiography/index.html [Accessed: January 25, 2018]

[15] Shope TB. Radiation-induced skin injuries from fluoroscopy. http://www.fda.gov/Radiation-EmittingProducts/RadiationEmittingProductsandProcedures/MedicalImaging/MedicalX-Rays/ucm116682.html U.S. Food and Drug Administration. Published September 1996

Chapter 4

Liver Directed Therapies

Edel Mendoza and Nadine Abi-Jaoudeh

Additional information is available at the end of the chapter

http://dx.doi.org/10.5772/intechopen.75163

Abstract

Minimally invasive liver directed therapies have established their role in the treatment of hepatic neoplasms. The Barcelona Clinic staging systems is the most widely used staging system and combines staging and management. While surgical resection or liver transplantation are commonly performed for very early stage cancers, patient's typically present with advanced disease. For those with single or small lesions, percutaneous tumor ablation may be curative. Transarterial chemoembolization or radioembolization are palliative treatments reserved for those with unresectable tumors or as bridge to transplant. In this chapter, we discuss the role of liver directed therapies throughout various stages of liver cancer, the management of these procedures, and its impact on patient care.

Keywords: hepatocellular carcinoma, colorectal cancer, percutaneous liver ablation chemoembolization, radioembolization, liver directed therapies

1. Introduction

Hepatocellular carcinoma (HCC) is the 5th leading cause of cancer in the US and 2nd most common cause of cancer related death worldwide [1]. HCC has a dismal prognosis with a ratio of mortality to incidence of 0.95 [2]. The incidence of HCC is rising as its primary risk factors, hepatitis B and C, become more prevalent in the population, especially in developing countries where hepatitis B is endemic [3]. The majority of patients with HCC are often diagnosed in intermediate or advanced stage disease where curative therapeutic options are no longer available [4]. Moreover, HCC is associated with liver cirrhosis, which also limits therapeutic options. The management of HCC is generally based on the guideline of the Barcelona Clinic Liver Cancer (BCLC) staging system. If HCC is detected in its early stages (BCLC-0 or BCLC-A), the 5-year survival may be as high 70–80% with optimal therapies such as resection, orthotopic liver

transplantation, or percutaneous ablation [5]. In the intermediate stage (BCLC-B), patients are managed with image-guided catheter based therapies such as transarterial embolization or chemoembolization (TAE/TACE). However, intra-arterial locoregional therapies are palliative and most patients experience disease progression. In 2017, several new therapeutic options have become available for advanced HCC although this is beyond the scope of this chapter where locoregional therapies will be reviewed.

2. Percutaneous ablation

Percutaneous ablation is a curative intent procedure reserved for patients with early stage disease HCC. It involves accessing the tumor percutaneously under ultrasound or CT guidance with probes. Three broad categories of percutaneous ablation exist: chemical, thermal, and non-thermal.

Chemical ablation induces cellular dehydration, protein denaturation, and blood vessel thrombosis causing coagulation necrosis via ethanol administration into the tumor. The ethanol has an unpredictable distribution in the surrounding tissue, leading to a high rate of tumor recurrence. This technique has largely been replaced by thermal ablation though still finds its uses where thermal ablation is risky such as in tumors in close proximity to vital organs.

Thermal ablation can be classified into three modalities: radiofrequency, microwave ablation, and cryoablation.

Radiofrequency ablation (RFA) is the most commonly performed procedure for hepatic tumors. There is an alternating electrical current within the device that causes agitated ions to generate heat and induce coagulative necrosis. This technique is reserved for tumors less than 3 cm due to the techniques poor conductive heating over greater distances.

Microwave ablation (MWA) uses electromagnetic waves to induce an alternating electrical field that produces heat. This has the ability to reach higher temperatures to overcome perfusion-mediated tissue cooling when compared to RFA, making ablation of larger tumors possible along with faster ablation times. This technique is preferred for tumors near major vessels, such as the inferior vena cava or main hepatic veins, due to the attenuated heat sink effect [6].

Cryoablation consists of pumping high-pressure argon into a probe, which escapes at the very tip and causes rapid expansion of the gas leading to intense cooling and formation of an ice ball around the needle tip. This causes intracellular ice crystals and disrupts the cell membrane and cellular metabolism. The low temperature also causes vascular thrombosis. Multiple cycles of freezing and thawing are performed. The advantage of cryoablation is the ability to see the ice ball during the procedure on CT, which allows the physician to determine adequate ablation. The technique was historically not used because of reported cryoshock. Recent reports have demonstrated that hepatic cryoablation is feasible and safe.

Non-thermal ablation is performed through irreversible electroporation (IRE). This technique involves high voltage electrical impulses between parallel electrodes. The high voltage causes

large pores in the cellular membranes leading to apoptosis. The advantage of IRE is the ability to ablate tumors that are in close proximity to vital structures such as the portal veins or bile ducts. IRE is a technically difficult procedure, as it requires multiple devices to be inserted in a near-perfect parallel conformation.

2.1. Management

Based on the BCLC, percutaneous ablation is reserved for patients with very early disease or early stage HCC that are not amenable to surgical resection or transplantation. The criteria for very early stage include a single tumor less than 2 cm. The criteria for early stage include a single tumor less than 5 cm or 3 nodules less than 3 cm each.

Absolute contraindications include intrahepatic biliary ductal dilatation, uncorrectable bleeding diathesis, or decompensated liver failure. Relative contraindications include tumor burden to be greater than five lesions, tumors larger than 3 cm, or tumors in close proximity to vital structures such as the portal vein, biliary tree, or gastrointestinal tract.

Patients are usually monitored for a few hours post-procedure. If vital signs and lab values are not significantly changed, patients can be discharged the same day or the day after the procedure. Follow up imaging with CT or MRI is obtained 4–8 weeks post procedure.

2.2. Complications

Major complications include intraperitoneal bleeding, intestinal perforation, bile duct stenosis, pneumothorax or hemothorax, liver abscess formation, or skin burns. Skin burns occur in less than 1% [7]. Late complication would include tumor seeding along the needle track which was found to occur 0.5% of cases with HCC based on a multicenter survey [8]. Other complications include minor symptoms such as pain, fever, or self-limited bleeding. The procedural mortality rate is between 0.1 and 0.5% which are due to sepsis, liver failure, portal venous thrombosis, or gastrointestinal perforation.

2.3. Results

In patients with HCC, RFA was shown to have complete tumor necrosis in 83% for lesions less than 3 cm and 88% for lesions in non-perivascular locations [9]. RFA had higher efficacy compared to ethanol ablation. The complete response rate is close to 97% with 5-year survival rates of 68% [10]. A study conducted by Cho et al. showed that RFA was just as effective as surgical resection for very early stage HCC [11]. A study conducted by Lencioni et al. showed that surgical resection remains the most effective treatment for patients with early stage HCC when compared to RFA [12]. A meta-analysis of over 21,000 patients demonstrated that surgery has higher post-operative mortality but improved 5 year overall survival compared to ablation. Of note, this study combined chemical and thermal ablation even though chemical ablation is known to be less efficient [13].

The studies comparing MWA to RFA have varying results. A study by Abdelaziz reported local recurrence rates of MWA, 3.9%, to be superior to RFA, 13.5%. Another study reported

decreased recurrence rates with RFA, 9%, compared to MWA, 19% [14]. A review of multiple studies demonstrate overall comparable rates for MWA and RFA in terms of overall survival and local recurrence.

A study by Wang compared cryoablation to RFA in patients with HCC lesions less than or equal to 4 cm. Results demonstrated significantly lower local tumor progression rates with cryoablation, 5.6%, compared to RFA, 10% [15]. For lesions larger than 3 cm, the difference became more apparent with progression rates of 7.7% for cryoablation and 18.2% for RFA. The recurrence free survival and overall survival rates were not significantly different between cryoablation and RFA [15].

In patients with metastatic CRC, RFA was shown to have a complete response rate of 91–97% [16]. In patients with five or fewer lesions less than 5 cm, the 5-year survival rate was between 24 and 44% [17]. For patients who had complete tumor ablation, 98% did not require further surgical resection either due to remaining disease free or developing disease progression [18].

3. Transarterial chemoembolization

Transarterial chemoembolization (TACE) is the most commonly performed procedure by interventional radiologists for treatment of unresectable hepatic malignancies. Nearly half of all HCC patients receive TACE at some point in their disease course [19]. Multiple techniques have been used for TACE over the past few decades.

The theory behind TACE relies on the liver's dual blood supply as hepatic tumors derive their blood supply mainly from the hepatic artery while normal hepatic parenchyma is predominantly supplied by the portal vein. Percutaneous access to the arterial system is obtained via femoral or radial artery catheterization. Imaging is performed to assess for variant anatomy, portal vein patency, and tumoral blood supply. Angiograms were performed, however in recent years, Cone Beam Computed Tomography (CBCT) has played an important role during locoregional therapies and is recommended as standard of care during chemoembolization [20]. Once the feeding arteries to the tumor are identified, they are selectively catheterized and chemoembolization is performed. Chemoembolization can be achieved by bland embolization, conventional trans-arterial chemoembolization (cTACE) or with drug-eluting embolic trans-arterial chemoembolization (DEE-TACE).

cTACE consists of administering chemotherapeutic agent(s) combined with an ethiodized oil emulsion followed by an embolic agent i.e. Gelfoam, or microspheres. Historically, doxorubicin, cisplatin, and mitomycin C in combination were used for cTACE, however due to shortage of some of the drugs, the regimens changed. Neither drug alone or any combination of these agents have shown to be statistically superior [17, 18]. Currently in the United States and Europe, doxorubicin is used in the majority of cases while miriplatin and cisplatin are used in Japan [21].

Lipiodol is an ethiodized oil that is commonly used for cTACE and has been considered the standard of care. The thick consistency allows it act as an embolic agent, which travels further into the microvascular than microspheres. In addition, lipiodol is radio-opaque and it

emulsifies the chemotherapeutic agents in oil droplets, which helps with drug delivery. In a meta-analysis of multiple randomized control trials, lipiodol was shown to be a safe, effective agent in the treatment of HCC [22].

Embolic microspheres loaded with doxorubicin for HCC or irinotecan for CRC are injected in the tumor feeding artery in DEE-TACE. Studies have shown slower, more sustained drug release with decreased systemic concentrations.

Bland embolization is also performed for HCC and neuroendocrine tumors. It can be accomplished either by injecting a mixture of Lipiodol and Gelfoam or with bland beads.

3.1. Indications and contraindications

The main role for TACE is reserved for patients with stage B disease based on the Barcelona Clinic Liver Cancer (BCLC) staging system. Stage B disease is defined as patients with large, multinodular disease with good functional status and a Child-Pugh A-B score. Other indications would include downstaging patient's tumor burden to allow for transplantation.

Absolute contraindications would be reserved for patients with poorly compensated advanced liver disease since TACE may exacerbate patient's symptoms and increase risks of progression into liver failure. Other absolute contraindications include refractory bleeding diathesis, large metastatic disease burden outside the liver, active infection, main, right and left portal vein thrombosis as well as refractory encephalopathy.

3.2. Management

TACE is commonly performed under moderate sedation. Pre-procedural hydration may be performed to decrease risk of contrast/chemotherapy-induced nephropathy. Pre-operative antibiotics are only given for patients with high risk for infection such as disrupted biliary drainage pathways.

Patients are usually admitted overnight post-procedure to monitor for potential complications. Most often, patients develop minor symptoms that can be managed medically such as post-embolization syndrome. This self-limiting syndrome is comprised of abdominal pain, fever, and nausea and usually occurs within the first 72 h post-procedure. This can be seen in up to 80% of patients. Post-procedural transaminitis is more frequent with cTACE compared to DEE-TACE.

Patients are typically discharged the next day. The criteria for discharge include appropriate pain control, ambulation, adequate urine production, and tolerating PO intake. TACE may be repeated for tumor control. Multiple treatments are often required until either the MRI shows greater than 90% tumor necrosis, the patient is downstaged, there is a lack of tumor response after at least two treatments, or the development of disease progression or a contraindication to treatment.

3.3. Complications

There are varying criteria in determining patients who are at high risk for post-TACE liver failure. High-risk patients include a total bilirubin greater than 2 mg/dL, INR greater than 1.5,

MELD score greater than 15, Child C disease, portal venous thrombosis, thrombocytopenia, or the presence of ascites. While many of these criteria have excluded patients in the past, advancements in technology has led to selective and superselective chemoembolization allowing a number of these patients to be treated. Non-selective chemoembolization can damage surrounding healthy hepatic parenchyma leading patients to decompensated liver failure, especially those with poor hepatic reserve. With selective and superselective techniques, there is increased sparing of viable tissue. Many articles have exhibited TACE being safely performed in high-risk patients. One study demonstrated the rate of selective TACE-related irreversible liver failure to be 3% compared to 20% in nonselective cases [23]. Other studies showed TACE to be safe and effective in patients with portal venous thrombosis, especially in those with hepatic reserve and collateral circulation [24]. Kothary et al. analyzed 65 high-risk TACE procedures which showed a procedure-related morbidity rate of 10.8% and a 30-day mortality rate of 7.7% [25]. Yoon et al. observed a procedure-related morbidity rate of 2% and a 30-day mortality rate of 1% in 96 high-risk patients [26]. Overall, the general consensus seems to be on a case-to-case basis in which baseline hepatic function, hepatic reserve, and overall tumor burden are commonly taken into account.

Non-target embolization can occur due to reflux of chemoembolic agents or failure to recognize the arterial anatomy supplying non-hepatic structures. This can lead to gastrointestinal ulceration/perforation, pancreatitis, cholecystitis, pneumonitis, or skin burns.

Hepatic abscess formation is rare in patients with unaltered anatomy. However, patients with post-surgical or disrupted anatomy of the biliary tree are at increased risk due to colonization of the biliary tree from enteric flora. One study showed 6 out of 7 patients with a prior bilioenteric anastomosis formed hepatic abscesses even after receiving standard broad spectrum prophylactic antibiotics [27]. Another study showed no formation of hepatic abscess in four patients with prior bilioenteric anastomosis when adding an aggressive bowel preparation [28]. In addition, gas formation within embolized hepatic tumors may occur post-procedurally which may lead to the misdiagnosis of a hepatic abscess.

Vascular complications are uncommon but include access site hematomas, pseudoaneurysms, or arteriovenous fistulas.

Other rare complications include sepsis, biliary strictures, variceal bleeding, renal failure, or chemotherapy-related toxicities such as alopecia, anemia, or myelosuppression.

3.4. Results

Multiple studies have shown TACE to increase overall survival when compared to conservative management. A randomized control trial by Llovet et al. was terminated early as it demonstrated the one-year and two-year survival rates for chemoembolization to be 82 and 63% compared to 63 and 27% for supportive care [29]. Another randomized trial by Lo et al. showed the one-year and two-year survival rates for chemoembolization to be 57 and 31% compared to 32 and 11% for supportive care [30]. Two meta-analyses of randomized controlled trials by Camma et al. and Llovet et al. showed a significant decrease in 2 year mortality with

TACE in patients with unresectable HCC (odds ratio 0.54, 95% CI 0.33–89, P = 0.015 and odds ratio 0.53, 95% CI 0.32–0.89, P = 0.017) [31].

Several studies have compared DEE-TACE versus cTACE versus bland TACE. The PRECISION V study was a prospective randomized study analyzing cTACE versus DEE-TACE. The study did not meet its primary endpoint of superior response rate with DEE-TACE but did show DEE-TACE is better tolerated [32]. One major criticism is that the study used 300–500 μ beads, which are considered large for this application. However other randomized controlled trials also compared cTACE versus DEE-TACE including Golfieri et al. This study on 177 patients did not show any statistical difference in terms of local or overall tumor response with 2 year follow-up but demonstrated reduced post procedural pain with DEE-TACE [33]. Meta-analysis on the topic has had equivocal results.

Interestingly, a randomized trial of 101 patients treated with TAE using microspheres alone versus TACE using doxorubicin-eluting microspheres found no difference in the response to treatment (primary endpoint) and no difference in overall survival [34].

A recent meta-analysis of randomized controlled trials pertaining to 5700 patients concluded that none of the transcatheter chemoembolization options as stand-alone were superior to transarterial bland embolization. The authors added that the conclusions are based on large information size of moderate quality based on data from 3 randomized controlled trials (RCT) of TAE versus best supportive care, 4 RCT of TAE versus TACE and 2 TAE versus DEB-TACE [35].

The SPACE trial, a randomized, double-blinded, phase II trial, compared Sorafenib with DEB-TACE versus DEB-TACE alone (placebo) in the treatment of intermediate stage HCC. The study did not show improvement in time to progression nor overall survival between the two groups [36].

4. Radioembolization

Radioembolization, also known as selective internal radiation therapy (SIRT), consists of administering either glass or resin microspheres loaded with radioactive isotope, yttrium-90 (Y-90). Y-90 is a pure better emitter with a half-life of 64.1 h and a mean tissue penetration of 2–3 mm. Radioembolization is currently not part of the standard treatment guidelines. However, promising clinical research has driven its growing use in the management of hepatic malignancies. A multidisciplinary team consisting of surgeons, interventional radiologist, hepatologists, oncologists, and radiation oncologists determines if a patient is a candidate for Y-90 radioembolization. The Barcelona Clinic Liver Cancer (BCLC) and Eastern Cooperative Oncology Group (ECOG) scoring systems are taken into account in the decision process. The microspheres used today are either glass and resin microspheres. Glass microspheres, or TheraSpheres, is FDA approved for the treatment of unresectable HCC. Resin microspheres, or SIR-Spheres, is premarket approved by the FDA for the treatment of hepatic metastases from colorectal cancer in combination with floxuridine. Glass microspheres carry a higher activity load, thus requiring decreased volumes and number of spheres, compared to resin microspheres for the same dose [37]. Since resin

microspheres require a higher volume, it would in theory produce a greater ischemic/embolic effect that would decrease the efficacy of delivering the full radiation dose. That being said, technical differences between the microspheres have not resulted in differences for overall survival in HCC [38]. Moreover computational studies comparing the resin and glass microspheres have demonstrated that particle trajectory in vessels have very little dependence on particle size. Indeed the authors concluded that the carrier fluid provides enough momentum to overcome the range of microspheres characteristics [39].

4.1. Indications and contraindications

Aside from the multidisciplinary approach, patients should have a life expectancy greater than 3 months with an ECOG status less than 2. Radioembolization is often used an adjuvant therapy to chemotherapy and/or salvage therapy after failure of first-line chemotherapy. This technique is also preferred in patients with portal vein thrombosis.

Absolute contraindications would include poor liver function with an elevated total bilirubin or increasing bilirubin, previous radiation to the liver, or significant hepatopulmonary lung shunting as that would lead to radiation pneumonitis. TARE should not be used as first line therapy in CRC and should be avoided in patients with extensive extra-hepatic disease burden.

4.2. Management

Radioembolization is usually performed in an outpatient setting. Pre-procedural angiogram and nuclear medicine Technetium macro-aggregated albumin (Tc-MAA) scan are necessary prior to treatment.

The angiogram determines anatomy including replaced right or left hepatic arteries. The origin of the right gastric should be identified. Coil embolization of any gastro-intestinal vessels originating from the right or left hepatic artery must be performed. Tc-MAA is needed to assess lung shunt fraction and consequently lung dose as tumor vascularity often have arteriovenous shunts. The lungs dose cannot exceed 30 Gy in one treatment session or 50 Gy cumulative dose [40]. Several strategies have been employed with high lung shunt fraction including no treatment, reduction of SIRsphere dose, bland embolization of the shunt, and balloon occlusion of the hepatic vein during microspheres delivery.

A 7–10 day course of proton pump inhibitors may be given to prevent gastric ulceration.

Post-procedural MRI should be obtained no earlier than 2 months to assess tumor response. In addition, tumor markers and liver function tests are obtained 4–6 weeks post-procedure.

Post-radioembolization syndrome is a constellation of abdominal pain, fatigue, nausea, vomiting, and fever. This is usually managed conservatively with hydration and over the counter medications.

4.3. Complications

Radioembolization induced liver disease (REILD) presents as jaundice, ascites without tumor progression, biliary obstruction, or elevated alkaline phosphatase. Histopathology reveals

veno-occlusive disease, sinusoidal congestion, and necrosis. REILD is defined as liver failure within 90 days post-radioembolization or greater than 90 days without tumor progression. Patients with decreased baseline liver function, with whole liver treatments and poly-chemotherapy are at increased risk [41]. Low-dose steroids and ursodeoxycholic acid can reduce the risk of REILD.

Non-target embolization may also occur with the adverse effects similar to TACE. Gastrointestinal ulceration remains a risk though with careful administration technique and proper coil embolization during work-up, complications are decreased to less than 4% [42]. Radiation pneumonitis if very rare occurring less than 1% and is avoidable with proper work up.

Other rare complications include radiation pancreatitis, dermatitis, cholecystitis or cholangitis. In general, biliary complications occur in less than 10% of cases though patients with polychemotherapy or disrupted ampulla of Vater patients are at increased risk [43].

Vascular complications are also similar to TACE. Patients on bevacizumab (Avastin) and other biologic agents (i.e. cetuximab, aflibercept, etc.) are at increased risk of dissection and rupture so careful technique and use of microcatheters should be employed.

Rarely lymphopenia may occur after glass microsphere radioembolization with greater than 25% decrease in lymphocyte count [43]. Fortunately, no opportunistic infections have been described.

4.4. Results

For HCC, the average response rate is between 35 and 47% with median survival of 15–24 months [44–47].

SARAH, an open-label, multicenter phase III trial (France), compared patients treated with SIRT versus Sorafenib alone in patients with unresectable HCC. SIRveNIB was an open label randomized controlled trial (Asia Pacific) that compared SIRT versus Sorafenib in locally advanced HCC. Both trials had a superiority design with overall survival as the primary endpoint. Both trials did not meet endpoint as there was no statistical difference in overall survival or progression-free survival. Indeed, overall survival was 8.0 months versus 9.9 months in the SARAH trial and 8.8 months versus 10 months in the SIRveNIB trial for SIRT and Sorafenib respectively [48]. However, patients treated with SIRT showed higher tumoral response rates, and increased quality of life in the intent to treat population which increased over time [49]. Moreover major criticism of these trials include inexperienced sites, a high TACE failure rate among patients, and 26.8% of the SIRT cohort in SARAH and 28.8% of the SIRT cohort in SIRveNIB did not receive SIRT as intended.

For metastatic colorectal cancer (mCRC) disease to the liver, the average response rate was between 35 and 43% with a median survival of 5–14 months [50]. TARE has demonstrated its role in second line or salvage therapy.

Three multi-center, randomized controlled phase III trials (FOXFIRE, SIRFLOX, and FOXFIRE-Global) examined the role of TARE (Y-90 resin microspheres) in combination with chemotherapy as first line therapy versus chemotherapy alone (FOLFOX or OxMdG) for liver-only or liver-dominant mCRC. Although an improvement of liver progression free survival was seen,

overall progression free survival was not altered and the combination of the three studies did not demonstrate an improvement of overall survival but an increase in adverse events with the combination [51]. Careful patient selection is necessary for proper integration of SIRT in the management of mCRC and it should not be performed as first line therapy.

Conflict of interest

None.

Author details

Edel Mendoza* and Nadine Abi-Jaoudeh

*Address all correspondence to: edelm@uci.edu

Department of Interventional Radiology, University of California, Irvine Medical Center, Orange, CA, USA

References

[1] Torre LA, Bray F, Siegel RL, Ferlay J, Lortet-tieulent J, Jemal A. Global cancer statistics, 2012. CA: a Cancer Journal for Clinicians. 2015;**65**(2):87-108. Available from: http://onlinelibrary.wiley.com/doi/10.3322/caac.21262/abstract

[2] Ferlay J, Soerjomataram I, Dikshit R, Eser S, Mathers C, Rebelo M, et al. Cancer incidence and mortality worldwide: Sources, methods and major patterns in GLOBOCAN 2012. International Journal of Cancer. 2015;**136**(5):E359-E386

[3] Zampino R, Boemio A, Sagnelli C, Alessio L, Adinolfi LE, Sagnelli E, et al. Hepatitis B virus burden in developing countries. World Journal of Gastroenterology. 2015;**21**(42): 11941-11953

[4] Bialecki ES, Di Bisceglie AM. Diagnosis of hepatocellular carcinoma. HPB: The Official Journal of the International Hepato Pancreato Biliary Association. 2005;**7**(1):26-34. Available from: http://www.ncbi.nlm.nih.gov/pubmed/18333158/%5Cnhttp://www.hpbonline.org/article/S1365-182X(15)30840-6/abstract%5Cnhttp://www.ncbi.nlm.nih.gov/pmc/articles/PMC2023919/%5Cnhttp://www.sciencedirect.com/science/article/pii/S1365182X15308406

[5] Saraswat VA, Pandey G, Shetty S. Treatment algorithms for managing hepatocellular carcinoma. Journal of Clinical and Experimental Hepatology. 2014;**4**:S80-S89

[6] Liang P, Wang Y. Microwave ablation of hepatocellular carcinoma. Oncology. 2007;**72**: 124-131

[7] Rhim H, Yoon KH, Lee JM, Cho Y, Cho JS, Kim SH, et al. Major complications after radio-frequency thermal ablation of hepatic tumors: Spectrum of imaging findings. Radiographics. 2003;**23**(1):123-126. Available from: http://www.ncbi.nlm.nih.gov/entrez/query.fcgi?cmd=Retrieve&db=PubMed&dopt=Citation&list_uids=12533647

[8] Livraghi T, Solbiati L, Meloni MF, Gazelle GS, Halpern EF, Goldberg SN. Treatment of focal liver Tumors with percutaneous radio-frequency ablation: Complications encountered in a Multicenter study. Radiology. 2003;**226**(2):441-451. Available from: http://pubs.rsna.org/doi/10.1148/radiol.2262012198

[9] Lu DSK, Yu NC, Raman SS, Limanond P, Lassman C, Murray K, et al. Radiofrequency ablation of hepatocellular carcinoma: Treatment success as defined by histologic examination of the explanted liver. Radiology. 2005;**234**(3):954-960

[10] Livraghi T, Meloni F, Di Stasi M, Rolle E, Solbiati L, Tinelli C, et al. Sustained complete response and complications rates after radiofrequency ablation of very early hepatocellular carcinoma in cirrhosis: Is resection still the treatment of choice? Hepatology. 2008; **47**(1):82-89

[11] Cho YK, Kim JK, Kim WT, Chung JW. Hepatic resection versus radiofrequency ablation for very early stage hepatocellular carcinoma: A markov model analysis. Hepatology. 2010;**51**(4):1284-1290

[12] Lencioni R, Crocetti L. Local-regional treatment of hepatocellular carcinoma. Radiology. 2012;**262**(1):43-58. Available from: http://www.ncbi.nlm.nih.gov/pubmed/22190656

[13] Ni J, Xu L, Sun H, Zhou J, Chen Y, Luo J. Percutaneous ablation therapy versus surgical resection in the treatment for early-stage hepatocellular carcinoma: A meta-analysis of 21,494 patients. Journal of Cancer Research and Clinical Oncology. 2013;**139**(12):2021-2033. Available from: http://link.springer.com/10.1007/s00432-013-1530-1

[14] Ohmoto K, Yoshioka N, Tomiyama Y, Shibata N, Kawase T, Yoshida K, et al. Comparison of therapeutic effects between radiofrequency ablation and percutaneous microwave coagulation therapy for small hepatocellular carcinomas. Journal of Gastroenterology and Hepatology. 2009;**24**(2):223-227. Available from: http://www.ncbi.nlm.nih.gov/pubmed/18823439

[15] Wang C, Wang HH, Yang W, Hu KK-Q, Xie H, Hu KK-Q, et al. Multicenter randomized controlled trial of percutaneous cryoablation versus radiofrequency ablation in hepatocellular carcinoma. Hepatology. 2015;**61**(5):1579-1590. Available from: http://www.ncbi.nlm.nih.gov/pubmed/25284802

[16] Lencioni R, Crocetti L, Cioni D, Della Pina C, Bartolozzi C. Percutaneous radiofrequency ablation of hepatic colorectal metastases: Technique, indications, results, and new promises. Investigative Radiology. 2004;**39**(11):689-697

[17] Solbiati L, Livraghi T, Goldberg SN, Ierace T, Meloni F, Dellanoce M, et al. Percutaneous radio-frequency ablation of hepatic metastases from colorectal cancer: Long-term results

in 117 patients. Radiology. 2001;**221**(1):159-166. Available from: http://www.ncbi.nlm.nih.gov/pubmed/11568334

[18] Livraghi T, Solbiati L, Meloni F, Ierace T, Goldberg SN, Gazelle GS. Percutaneous radiofrequency ablation of liver metastases in potential candidates for resection: The "test-of-time" approach. Cancer. 2003;**97**(12):3027-3035

[19] Geschwind J-F, Kudo M, Marrero JA, Venook AP, Chen X-P, Bronowicki J-P, et al. TACE treatment in patients with Sorafenib-treated unresectable hepatocellular carcinoma in clinical practice: Final analysis of GIDEON. Radiology. 2016;**279**(2):630-640. Available from: http://pubs.rsna.org/doi/10.1148/radiol.2015150667

[20] de Baere T, Arai Y, Lencioni R, Geschwind JF, Rilling W, Salem R, et al. Treatment of liver tumors with lipiodol TACE: Technical recommendations from experts opinion. Cardiovascular and Interventional Radiology. 2016;**39**(3):334-343

[21] Horikawa M, Miyayama S, Irie T, Kaji T, Arai Y. Development of conventional transarterial chemoembolization for hepatocellular carcinomas in Japan: Historical, strategic, and technical review. American Journal of Roentgenology. 2015;**205**(4):764-773

[22] Lencioni R, de Baere T, Soulen MC, Rilling WS, Geschwind JFH. Lipiodol transarterial chemoembolization for hepatocellular carcinoma: A systematic review of efficacy and safety data. Hepatology. 2016;**64**(1):106-116

[23] Chan AO, Yuen MF, Hui CK, Tso WK, Lai CL. A prospective study regarding the complications of transcatheter intraarterial lipiodol chemoembolization in patients with hepatocellular carcinoma. Cancer. 2002;**94**(6):1747-1752

[24] Luo J, Guo R-P, Lai ECH, Zhang Y-J, Lau WY, Chen M-S, et al. Transarterial chemoembolization for unresectable hepatocellular carcinoma with portal vein tumor thrombosis: A prospective comparative study. Annals of Surgical Oncology. 2011;**18**(2):413-420. Available from: http://www.springerlink.com/index/10.1245/s10434-010-1321-8

[25] Kothary N, Weintraub JL, Susman J, Rundback JH. Transarterial chemoembolization for primary hepatocellular carcinoma in patients at high risk. Journal of Vascular and Interventional Radiology. 2007;**18**(12):1517-1526. quiz 1527

[26] Yoon HJ, Kim JH, Kim KA, Lee IS, Ko GY, Song HY, et al. Transcatheter arterial chemolipiodol infusion for unresectable hepatocellular carcinoma in 96 high-risk patients. Clinical Radiology. 2010;**65**(4):271-277

[27] Kim W, Clark TW, Baum RA, Soulen MC. Risk factors for liver abscess formation after hepatic chemoembolization. Journal of Vascular and Interventional Radiology. 2001;**12**(8):965-968. Available from: http://www.ncbi.nlm.nih.gov/pubmed/11487677

[28] Geschwind J-FH, Kaushik S, Ramsey DE, Choti MA, Fishman EK, Kobeiter H. Influence of a new prophylactic antibiotic therapy on the incidence of liver abscesses after chemoembolization treatment of liver tumors. Journal of Vascular and Interventional Radiology. 2002;**13**(11):1163-1166. Available from: http://www.ncbi.nlm.nih.gov/pu bmed/12427817

[29] Llovet JM, Real MI, Montaña X, Planas R, Coll S, Aponte J, et al. Arterial embolisation or chemoembolisation versus symptomatic treatment in patients with unresectable hepatocellular carcinoma: A randomised controlled trial. Lancet (London, England). 2002;**359**(9319):1734-1739. Available from: http://www.ncbi.nlm.nih.gov/pubmed/12049862

[30] Lo CM, Ngan H, Tso WK, Liu CL, Lam CM, Poon RTP, et al. Randomized controlled trial of transarterial Lipiodol chemoembolization for unresectable hepatocellular carcinoma. Hepatology. 2002;**35**(5):1164-1171

[31] Cammà C, Schepis F, Orlando A, Albanese M, Shahied L, Trevisani F, et al. Transarterial chemoembolization for unresectable hepatocellular carcinoma: Meta-analysis of randomized controlled trials. Radiology. 2002;**224**(1):47-54. Available from: http://pubs.rsna.org/doi/10.1148/radiol.2241011262

[32] Lammer J, Malagari K, Vogl T, Pilleul F, Denys A, Watkinson A, et al. Prospective randomized study of doxorubicin-eluting-bead embolization in the treatment of hepatocellular carcinoma: Results of the PRECISION v study. Cardiovascular and Interventional Radiology. 2010;**33**(1):41-52

[33] Golfieri R, Giampalma E, Renzulli M, Cioni R, Bargellini I, Bartolozzi C, et al. Randomised controlled trial of doxorubicin-eluting beads vs conventional chemoembolisation for hepatocellular carcinoma. British Journal of Cancer. 2014;**111**(2):255-264

[34] Brown KT, Do RK, Gonen M, Covey AM, Getrajdman GI, Sofocleous CT, et al. Randomized trial of hepatic artery embolization for hepatocellular carcinoma using doxorubicin-eluting microspheres compared with embolization with microspheres alone. Journal of Clinical Oncology. 2016;**34**(17):2046-2053

[35] Katsanos K, Kitrou P, Spiliopoulos S, Maroulis I, Petsas T, Karnabatidis D. Comparative effectiveness of different transarterial embolization therapies alone or in combination with local ablative or adjuvant systemic treatments for unresectable hepatocellular carcinoma: A network meta-analysis of randomized controlled trials. Lu S-N, ed. PLoS ONE. 2017;**12**(9):e0184597

[36] Lencioni R, Llovet JM, Han G, Tak WY, Yang J, Guglielmi A, et al. Sorafenib or placebo plus TACE with doxorubicin-eluting beads for intermediate stage HCC: The SPACE trial. Journal of Hepatology. 2016;**64**(5):1090-1098

[37] Edeline J, Gilabert M, Garin E, Boucher E, Raoul JL. Yttrium-90 microsphere radioembolization for hepatocellular carcinoma. Liver Cancer. 2015;**4**(1):16-25

[38] Sangro B, Iñarrairaegui M. Radioembolization for hepatocellular carcinoma: Evidence-based answers to frequently asked questions. Journal of Nuclear Medicine and Radiation Therapy. 2011;**2**:110

[39] Basciano CA, Kleinstreuer C, Kennedy AS, Dezarn WA, Childress E. Computer modeling of controlled microsphere release and targeting in a representative hepatic artery system. Annals of Biomedical Engineering. 2010;**38**(5):1862-1879

[40] Ho S, Lau WY, Leung TWT, Chan M, Johnson PJ, Li AKC. Clinical evaluation of the partition model for estimating radiation doses from yttrium-90 microspheres in the treatment of hepatic cancer. European Journal of Nuclear Medicine. 1997;**24**(3): 293-298

[41] Gil-Alzugaray B, Chopitea A, Iñarrairaegui M, Bilbao JI, Rodriguez-Fraile M, Rodriguez J, et al. Prognostic factors and prevention of radioembolization-induced liver disease. Hepatology. 2013;**57**(3):1078-1087

[42] Lam MGEH, Banerjee S, Louie JD, Abdelmaksoud MHK, Iagaru AH, Ennen RE, et al. Root cause analysis of gastroduodenal ulceration after yttrium-90 radioembolization. Cardiovascular and Interventional Radiology. 2013;**36**(6):1536-1547

[43] Riaz A, Awais R, Salem R. Side effects of yttrium-90 radioembolization. Frontiers in Oncology. 2014;**4**:198. Available from: http://journal.frontiersin.org/article/10.3389/fonc.2014.00198/

[44] Kulik LM, Atassi B, Van Holsbeeck L, Souman T, Lewandowski RJ, Mulcahy MF, et al. Yttrium-90 microspheres (TheraSphere®) treatment of unresectable hepatocellular carcinoma: Downstaging to resection, RFA and bridge to transplantation. Journal of Surgical Oncology. 2006;**94**(7):572-586

[45] Salem R, Lewandowski RJ, Atassi B, Gordon SC, Gates VL, Barakat O, et al. Treatment of unresectable hepatocellular carcinoma with use of 90Y microspheres (therasphere): Safety, tumor response, and survival. Journal of Vascular and Interventional Radiology. 2005; **16**(12):1627-1639

[46] Geschwind JFH, Salem R, Carr BI, Soulen MC, Thurston KG, Goin KA, et al. Yttrium-90 microspheres for the treatment of hepatocellular carcinoma. Gastroenterology. 2004

[47] Lau WY, Ho S, Leung TWT, Chan M, Ho R, Johnson PJ, et al. Selective internal radiation therapy for nonresectable hepatocellular carcinoma with intraarterial infusion of 90yttrium microspheres. International Journal of Radiation Oncology, Biology, Physics. 1998;**40**(3): 583-592

[48] PHW C, Gandhi M. Phase III multi-centre open-label randomized controlled trial of selective internal radiation therapy (SIRT) versus sorafenib in locally advanced hepatocellular carcinoma: The SIRveNIB study. Journal of Clinical Oncology. 2017 May;**35**(15_suppl):4002. Available from: http://ascopubs.org/doi/abs/10.1200/JCO.2017.35.15_suppl.4002

[49] Vilgrain V, Abdel-Rehim M, Sibert A, Ronot M, Lebtahi R, Castéra L, et al. Radioembolisation with yttrium–90 microspheres versus sorafenib for treatment of advanced hepatocellular carcinoma (SARAH): Study protocol for a randomised controlled trial. Trials. 2014;**15**:474

[50] Kennedy AS, Coldwell D, Nutting C, Murthy R, Wertman DE, Loehr SP, et al. Resin 90Y-microsphere brachytherapy for unresectable colorectal liver metastases: Modern

USA experience. International Journal of Radiation Oncology, Biology, Physics. 2006; **65**(2):412-425

[51] Wasan HS, Gibbs P, Sharma NK, Taieb J, Heinemann V, Ricke J, et al. First-line selective internal radiotherapy plus chemotherapy versus chemotherapy alone in patients with liver metastases from colorectal cancer (FOXFIRE, SIRFLOX, and FOXFIRE-global): A combined analysis of three multicentre, randomised, phase 3 trials. The Lancet Oncology. 2017;**18**(9):1159-1171

Chapter 5

State-Of-The-Art X-Ray Digital Tomosynthesis Imaging

Tsutomu Gomi

Additional information is available at the end of the chapter

http://dx.doi.org/10.5772/intechopen.81667

Abstract

Digital tomosynthesis (DT) is a notable modality in medical imaging because it shows the spread of the target area with lower radiation dose relative to computed tomography. In this section, we describe the technique in two parts: (1) image quality (contrast) and (2) DT image reconstruction algorithms, including state-of-the-art total variation minimization reconstruction algorithms with single-energy X-ray conventional polychromatic imaging and novel dual-energy (DE) virtual monochromatic imaging. The novel DE virtual monochromatic image-processing algorithm provides adequate overall performance (especially, reduction of beam-hardening, reduction of noise). The DE virtual monochromatic image-processing algorithm appears to be a promising new option for imaging in DT because it provides three-dimensional visualizations of high-contrast images that are far superior to those of images processed by using conventional single-energy polychromatic image-processing algorithms.

Keywords: tomosynthesis, reconstruction, virtual monochromatic imaging, polychromatic imaging, dual-energy imaging

1. Introduction

Approximately 30 years have passed since Dr. Hounsfield developed a practical computed tomography (CT) system. The arrival of CT devices in the field of medical diagnosis has led to a revolution equivalent to the discovery of X-rays by Dr. Roentgen. Since then, most researchers who aim to improve medical diagnosis quality have worked toward the functional improvement of CT instruments, thus leading to the development of fan-beam CT, helical scan CT, multislice CT, and cone-beam CT instruments. These new instruments reduce the time needed for image reconstruction and significantly improve image quality. Given the increasing demand for better technology, there has been continued research and development of high-performance CT instruments.

Interest in digital tomosynthesis (DT) and its clinical applications has been revived by recent advances in digital X-ray detector technology. Conventional tomography technology provides planar information about an object from its projection images. In tomography, an X-ray tube and an X-ray film receptor lie on either side of the object. The relative motion of the tube and film is predetermined on the basis of the location of the in-focus plane [1]. A single image plane is generated by a scan, and multiple scans are required to provide a sufficient number of planes to cover the selected structure in the object. DT acquires only one set of discrete X-ray projections that can be used to reconstruct any plane of the object retrospectively [2]. The technique has been investigated in angiography and in the imaging of the chest, hand joints, lungs, teeth, and breasts [3–8]. Dobbins et al. [9] reviewed DT and showed that it outperformed planar imaging to a statistically significant extent. Various types of DT reconstruction methods have been explored.

Current DT mainly involves image acquisition/reconstruction using polychromatic imaging. Material decomposition or virtual monochromatic image processing using dual energy (DE) has been studied in CT, and many basic and clinically useful applications have been reported [10–12]. Similar to CT, it can be expected that DT also benefits from image quality improvements. In this chapter, the fundamental image quality characteristics of various reconstruction algorithms (including a state-of-the-art reconstruction algorithm) using polychromatic imaging and virtual monochromatic DT imaging that were verified in phantom experiments are discussed.

2. DT reconstruction

Existing tomosynthesis algorithms can be divided into three categories: (1) backprojection (BP), (2) filtered backprojection (FBP), and (3) iterative reconstruction (IR) algorithms.

2.1. BP

The BP algorithm is referred to as "shift-and-add" (SAA) [9], whereby projection images taken at different angles are electronically shifted and added to generate an image plane focused at a certain depth below the surface. The projection shift is adjusted such that the visibility of the features in the selected plane is enhanced, whereas those in other planes are blurred. By using a digital detector, the image planes at all depths can be retrospectively reconstructed from one set of projections. The SAA algorithm is valid only if the motion of the X-ray focal spot is parallel to the detector.

2.2. FBP

FBP algorithms are widely used in CT when many projections acquired at >360° are used to reconstruct cross-sectional images. The number of projections typically ranges from a few hundred to approximately 1000. The Fourier central slice theorem is fundamental to FBP theory. In two-dimensional (2D) CT imaging, a projection of an object corresponds to sampling that object along the direction perpendicular to the X-ray beam in the Fourier space [13]. For

many projections, information about the object is well sampled, and the object can be restored by combining the information from all projections.

In three-dimensional (3D) cone-beam imaging, information about the object in Fourier space is related to the Radon transform of the object. The relationship between the Radon transform and cone-beam projections has been well studied, and solutions to the cone-beam reconstruction have been provided [14, 15]. The Feldkamp algorithm generally provides a high degree of precision for 3D reconstruction images when an exact type of algorithm is employed [16]. Therefore, this method has been adopted for the image reconstruction of 3D tomography and multidetector cone-beam CT. A number of improved 3D reconstruction methods have been derived from the Feldkamp algorithm.

We denoted the intensity of the incident X-rays as $I_0 = (\delta, c, d)$ and that of the X-rays that passed through the structure at the location (δ, c, d) as $I = (\delta, c, d)$. The image data $d^F = (\delta, c, d)$ were calculated as follows:

$$d^F(\delta, c, d) = ln\, \frac{I_0(\delta, c, d)}{I(\delta, c, d)} \tag{1}$$

The original projection data are used to generate an FBP image:

$$f^{FDK} = \int_{-\theta}^{\theta} \frac{R^2}{U^2} \tilde{d}F(\delta, c, d) D\delta \tag{2}$$

$$U(X, Y, \delta) = R + X\cos\delta + Y\sin\delta$$

$$c(X, Y, \delta) = R\frac{-X\sin\delta + Y\cos\delta}{R + X\cos\delta + Y\sin\delta}$$

$$d(X, Y, Z, \delta) = Z\frac{R}{R + X\cos\delta + Y\sin\delta}$$

$$\tilde{d}F(\delta, c, d) = \left(\frac{R}{\sqrt{R^2 + c^2 + d^2}} d^F(\delta, c, d)\right) * g^P(\gamma)$$

where the projection angle δ, fan-angle γ, source trajectory R, acquisition angle θ, and $g^p(\gamma)$ represent a convolution with the Ramachandran–Lakshminarayanan filter. The Ramachandran–Lakshminarayanan (ramp) filter is shown below:

$$g^p(\gamma) = \left(\frac{\gamma}{sin\,\alpha}\right)^2 \tag{3}$$

2.3. IR

An IR algorithm performs the reconstruction in a recursive fashion [17, 18], unlike the one-step operation in backprojection and FBP algorithms. During IR, a 3D object model is repeatedly

updated until it converges to the solution that optimizes an objective function. The objective function defines the criteria of the reconstruction solution.

Algebraic reconstruction methods assume that the image is an array of unknowns, and the reconstruction problem can be established as a system of linear equations. The unknowns of this system are approximated with respect to the ray sums iteratively [17, 18]. In each iteration, current reconstruction is reprojected and updated according to how much it satisfies the projection measurements.

$$G_{\mathrm{x}} = f \tag{4}$$

In the DT reconstruction, x represents the pixel values for $\mathrm{x} \in \Re^N$, whereas f represents the observed data for $f \in \Re^M$. The weighting value $G \in \Re^{M \times N}$ was created by using a forward projection, and the matrix G combines the submatrices of each projection. G_{mn} is defined as the length of intersection of the m^{th} ray with the n^{th} cell. DT reconstruction starts with an initial guess x^0 and computes x^1 by projecting x^0 onto the first hyperplane in Eq. 4. The algebraic reconstruction technique (ART) update procedure (or error correction) is shown below:

$$\vec{\mathrm{x}}^{(k)} = \vec{\mathrm{x}}^{(k-1)} + \beta \frac{b_i - \vec{a}_i \vec{\mathrm{x}}^{(k-1)}}{\left\| \vec{a}_i \right\|^2} \vec{a}_i \tag{5}$$

where $\vec{a_i} = (a_{i1}, a_{i2}, \ldots, a_{in})$ is the ith row of the projection matrix, and β is the relaxation parameter (1.0). $\left\| \vec{a}_i \right\|^2$ is the normalization factor. The update is performed for each projection measurement bi separately, that is, the kth iteration consists of a sweep through the m projection measurements. The algorithm iterates through the equations periodically; therefore, $i = (i\text{-}1) \bmod (m) + 1$.

The ART algorithm updates the image vector per ray such that the update satisfies only a single equation representing the corresponding ray integral. By contrast, the simultaneous IR technique (SIRT) algorithm updates the image vector after all equations are considered. The update procedure of SIRT is given in Eq. 6 according to [19].

$$\vec{\mathrm{x}}^{(k)} = \vec{\mathrm{x}}^{(k-1)} + \beta \frac{1}{\sum_i^m a_{ij}} \sum_i^m a_{ij} \frac{b_i - \vec{a}_i \vec{\mathrm{x}}^{(k-1)}}{\sum_{j=1}^n a_{ij}} \tag{6}$$

The simultaneous ART (SART) algorithm [20] is proposed as a combination of the ART and SIRT algorithms. SART updates the superior implementation of ART and is based on a simultaneous update of the current reconstruction similar to SIRT. In the SART algorithm, the update procedure is applied for all rays in a given scan direction (projection) instead of each ray separately (similar to conventional ART) or instead of all rays simultaneously (similar to SIRT). The SART update is expressed as follows:

$$\vec{x}^{(k)} = \vec{x}^{(k-1)} + \beta \frac{1}{\sum_{i \in \Omega_t} a_{ij}} \sum_{i \in \Omega_t} a_{ij} \frac{b_i - \vec{a}_i \vec{x}^{(k-1)}}{\sum_{j=1}^{n} a_{ij}} \tag{7}$$

where Ω_t is the set of indices of the rays sent from the tth projection direction.

The objective function in the maximum likelihood expectation–maximization (MLEM) algorithm is the likelihood function, which is the probability of obtaining the measured projections in a given object model. The solution of the MLEM algorithm is an object model that maximizes the probability of obtaining the measured projections.

The transition matrix $\alpha(i,j)$ represents the probability for an event generated in the area of the source covered by pixel i to be detected. The count registered by the detector is represented by the vector $y(j) = [y(1), y(2), y(3),..., y(J)]$:

$$x^{(k+1)}(i) = x^{(k)}(i) C^{(k)}(i) \tag{8}$$

$$C^{(k)}(i) = \frac{1}{\sum_{j=1}^{n} \alpha(i,j)} \sum_{j=1}^{J} \frac{y(j)}{\sum_{i=1}^{n} \alpha(i,j) x^{(k)}(i)} \alpha(i,j) \tag{9}$$

$$x^{(k+1)}(i) = \frac{1}{\sum_{j=1}^{n} \alpha(i,j)} x^{(k)}(i) \sum_{j=1}^{J} \frac{y(j)\alpha(i,j)}{\sum_{i=1}^{n} x^{(k)} \alpha(i,j)} \tag{10}$$

$i = 1, 2, \ldots, n.$

2.4. Total variation minimization reconstruction algorithm

An iterative algorithm using total variation (TV)-based compressive sensing was recently developed for volume image reconstruction from a tomographic scan [21]. The image TV has been used as a penalty term in iterative image reconstruction algorithms [21]. The TV of an image is defined as the sum of the first-order derivative magnitudes for all pixels in the image. TV minimization is an image domain optimization method associated with compressed sensing theory [21]. As TV-minimization IR for image reconstruction, the TV-minimization IR technique is the SART [20] with algebraic IR for constraining the TV-minimization problem, which is called SART-TV [21]. In TV-minimization IR, adding a penalty to the data–fidelity–objective function tends to smooth out noise in the image while preserving edges within the image [21–25].

SART-TV minimizes the Rudin, Osher, and Fatemi (ROF) model [26], that is, SART-TV also takes into account the image information when minimizing the TV of the image. If only the TV-minimization step was performed in the rest of the algorithms, the result would be a flat image; alternatively, the ROF model ensures that the image does not change considerably. The SART-TV optimal parameters include the iteration number for TV minimization [100 (np)] and the length of each gradient-descent step [50 (q)]. These optimal parameters have been

shown to be very relevant to image quality [21, 24]. In our study, we minimized the image quality by using these optimal parameters for the SART-TV algorithms.

The SART-TV algorithm is expressed in the form of a pseudo code as follows:

$$\beta = 1.0;\ np; 100\ q; 50$$

$$\vec{x} = 0$$

repeat *main loop*

$$\vec{x_0} = \vec{x}$$

(*SART*)

$$\text{for } i = 1 : N_d, \quad \vec{x} = \vec{x} + \beta \frac{1}{\sum_{i \in \Omega_i} A_{ij}} \sum_{i \in \Omega_i} A_{ij} \frac{b_i - \vec{A_i} \cdot \vec{x}}{\sum_{j=1}^{n} A_{ij}}$$

$$\text{for } i = 1 : N_i, \ \text{ if } x_i < 0 \text{ then } x_i = 0$$

(*enforce positivity*)

$$\vec{x_{res}} = \vec{x}$$

for i = 1:np do *TV-minimization loop*

$$\Delta x = \left| \vec{x} - \vec{x}_0 \right|$$

$$\vec{d}x = \nabla_{\vec{x}} \left\| \vec{x} \right\|_{TV}$$

$$\hat{d}x = \vec{d}x \Big/ \left| \vec{d}x \right|$$

$$\vec{x} = \vec{x} - q^* \Delta x^* \hat{d}x$$

end

$$\text{return } \vec{x}_{res}$$

3. Phantom specification

For the evaluation of low-contrast resolution, a contrast-detail (CD) phantom was used with epoxy slabs. The CD phantoms of different diameters (signal region, $CaCO_3$) and thicknesses were arranged within the epoxy slabs. For X-ray imaging, we placed polymethyl methacrylate (PMMA) slabs (200 × 200 mm) with 50 mm thickness on the top of the CD phantom (**Figure 1**).

http://dx.doi.org/10.5772/intechopen.81667

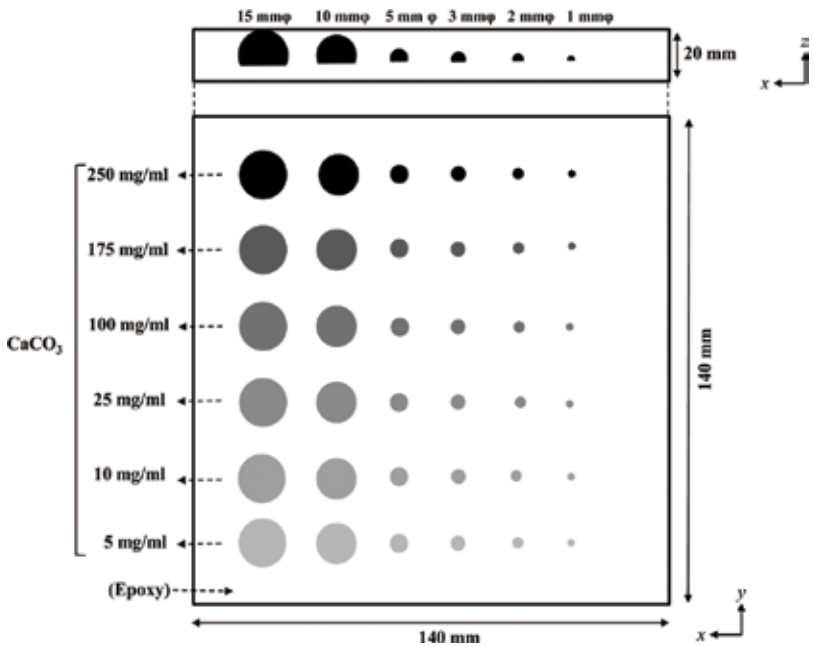

Figure 1. Illustration of the CD phantom used in this study.

4. Virtual monochromatic DT imaging using DE

4.1. Theory of material decomposition processing

Given that the photoelectric effect and Compton scattering of X-ray photons in the diagnostic range (E < 140 keV) are the predominant mechanisms responsible for X-ray attenuation (monochromatic X-ray), the mass attenuation coefficient of any material can be expressed with sufficient accuracy as a linear combination of the photoelectric and Compton attenuation coefficients. Consequently, the mass attenuation coefficient can also be expressed as a linear combination of the attenuation coefficients of two basis materials [10]:

$$\mu(r,E) = \left(\frac{\mu}{\rho}\right)_1 (E) \cdot \rho_1(r) + \left(\frac{\mu}{\rho}\right)_2 (E) \cdot \rho_2(r) \tag{11}$$

where the basis materials exhibit different photoelectric and Compton characteristics, $(\mu/\rho)_i(E)$ and i = 1, 2 denote the mass attenuation coefficients of the two basis materials, and $\rho_i(r)$ and i = 1, 2 denotes the local densities (g/cm^3) of the two basis materials at location *r*.

In principle, DE can only accurately decompose a mixture into two materials. Therefore, for DE measurement–based mixture decomposition into three constitutive materials, a third constituent must be provided to solve for three unknowns by using only two spectral measurements. In one solution, the sum of the volumes of the three constituent materials is assumed to be

equivalent to the volume of the mixture (volume or mass conservation) [11]. In this work, we used a simple projection space (prereconstruction) decomposition method to estimate the material fractions (f_n) of the $CaCO_3$ (f_{caco3}, local density; 2.711 g/cm^3), PMMA (f_{PMMA}, local density; 1.17 g/cm^3), and epoxy resin (f_{epoxy}, local density; 1.11 g/cm^3) in the phantom.

Three basis materials can also be expressed as a linear combination of the attenuation coefficients:

$$\mu(r,E) = \left(\frac{\mu}{\rho}\right)_1 (E)\cdot\rho_1(r) + \left(\frac{\mu}{\rho}\right)_2 (E)\cdot\rho_2(r) + \left(\frac{\mu}{\rho}\right)_3 (E)\cdot\rho_3(r) \tag{12}$$

In DE acquisition, the detected image intensity can be expressed as follows:

$$I_L = \int P_L(E)\, exp\left\{-\left(\frac{\mu}{\rho}\right)_1 (E)\cdot L_1 - \left(\frac{\mu}{\rho}\right)_2 (E)\cdot L_2 - \left(\frac{\mu}{\rho}\right)_3 (E)\cdot L_3\right\} dE \tag{13}$$

$$I_H = \int P_H(E)\, exp\left\{-\left(\frac{\mu}{\rho}\right)_1 (E)\cdot L_1 - \left(\frac{\mu}{\rho}\right)_2 (E)\cdot L_2 - \left(\frac{\mu}{\rho}\right)_3 (E)\cdot L_3\right\} dE \tag{14}$$

$$L_1{}^* L_2{}^* L_3 = 1.0 \tag{15}$$

$$L_1 = \int \rho_1(r)dl$$

$$L_2 = \int \rho_2(r)dl$$

$$L_3 = \int \rho_3(r)dl$$

where $P_L(E)$ represents the low-energy primary intensities, $P_H(E)$ represents the high-energy primary intensities, I_L represents the low-energy attenuated intensities, and I_H denotes the high-energy attenuated intensities. The equivalent densities (g/cm^2; L_1, L_2, and L_3) of the three basis materials must be determined for each ray path. Eqs. (13, 14, 15) can be solved for the equivalent area density, where L_1, L_2, and L_3 are the unknown materials. Therefore, the basis material decomposition can be accomplished by solving simultaneous equations to calculate the values of L_1, L_2, and L_3 from the measured projection pixel values [12]. By using the density corresponding to the area with the three basis materials, the linear attenuation coefficient $\mu(r, E)$ can be calculated for any photon.

We used the local and area densities for each material to calculate the theoretical linear attenuation coefficient curves shown in **Figure 2**; these values were generated by inputting the chemical compositions of the $CaCO_3$, epoxy resin, and PMMA into the XCOM program developed by Berger and Hubbell [27]. The curves show that the linear attenuation coefficient of $CaCO_3$ decreases more rapidly than those of the foam epoxy and PMMA in the energy band <100 keV. Finally, we used the projection space decomposition approach to generate material decomposition images for the $CaCO_3$, epoxy resin image, and PMMA by using the following process.

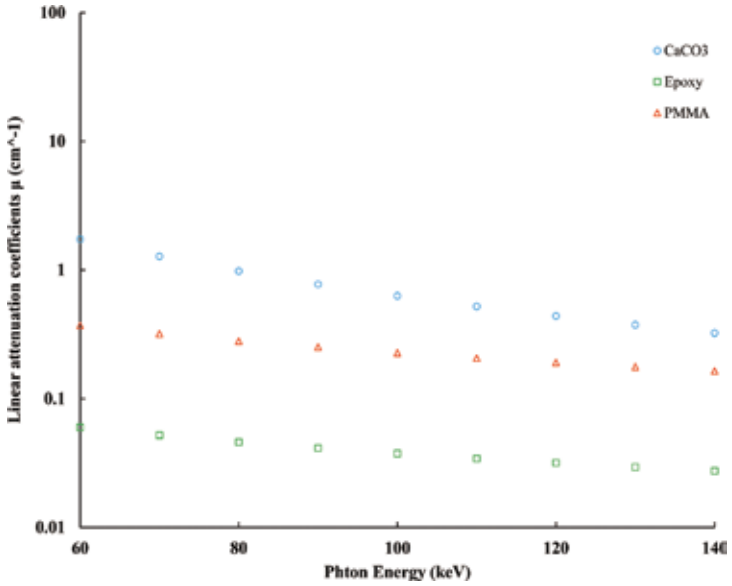

Figure 2. The linear attenuation coefficients of $CaCO_3$, epoxy, and PMMA with respect to the photons.

Eqs. (13) and (14) were used to calculate the values for I_{L_caco3}, I_{L_PMMAr}, I_{L_epoxy}, I_{H_caco3}, I_{H_PMMA}, and I_{H_epoxy} as simulated attenuation intensities of these materials at the two energy levels. These values were then used to construct a sensitivity matrix, and the material fractions were obtained from the inverse of this matrix (Eq. 16):

$$\begin{bmatrix} f_{CaCO3} \\ f_{PMMA} \\ f_{epoxy} \end{bmatrix} = \begin{bmatrix} I_{L\_CaCO3} & I_{L\_PMMA} & I_{L\_epoxy} \\ I_{H\_CaCO3} & I_{H\_PMMA} & I_{H\_epoxy} \\ 1.0 & 1.0 & 1.0 \end{bmatrix}^{-1} \begin{bmatrix} DT_{EL} \\ DT_{EH} \\ 1.0 \end{bmatrix} \tag{16}$$

$$f_{CaCO3} I_{L\_CaCO3} + f_{PMMA} I_{L\_PMMA} + f_{epoxy} I_{L\_epoxy} = DT_{EL}$$

$$f_{CaCO3} I_{H\_CaCO3} + f_{PMMA} I_{H\_PMMA} + f_{epoxy} I_{H\_epoxy} = DT_{EH}$$

$$f_{CaCO3} + f_{PMMA} + f_{epoxy} = 1.0$$

4.2. Virtual monochromatic image processing

After decomposition by matrix inversion, the "*inv*" function available in MATLAB was used (Mathworks; Natick, MA, USA); this function constrains the possible fraction to [0,1] while imposing a sum of one. Accordingly, the processing pipeline yields three material fraction outputs corresponding to $CaCO_3$, epoxy, and PMMA.

Virtual monochromatic processing is performed according to Eq. 15:

$$Mono\_p\_img = f_{CaCO3}{}^{*}\left(\frac{\mu}{\rho}\right)_{CaCO3}(E) + f_{PMMA}{}^{*}\left(\frac{\mu}{\rho}\right)_{PMMA}(E) + f_{epoxy}{}^{*}\left(\frac{\mu}{\rho}\right)_{epoxy}(E) \quad (17)$$

where *Mono_p_img* is the virtual monochromatic projection image, and $[\mu/\rho]_{caco3}(E)$, $[\mu/\rho]_{PMMA}(E)$, and $[\mu/\rho]_{epoxy}(E)$ are the mass attenuation coefficients of each material. The generated virtual monochromatic X-ray projection image was reconstructed by using each algorithm for energies of 60, 80, 100, 120, and 140 keV. The real projection data acquired on a DT system were used for reconstruction. All image reconstruction calculations, including DE material decomposition processing and reconstruction, as well as FBP, SART, SART-TV, virtual monochromatic processing, and MLEM, were implemented in MATLAB.

5. DT system

5.1. DT overview

The DT system (SonialVision Safire II; Shimadzu Co., Kyoto, Japan) comprised an X-ray tube [anode: tungsten with rhenium and molybdenum; real filter: inherent; aluminum (1.1 mm), additional; aluminum (0.9 mm), and copper (0.1 mm)] with a 0.4 mm focal spot and 362.88 × 362.88 mm amorphous selenium digital flat-panel detector (detector element, 150 × 150 μm^2). The source-to-isocenter and isocenter-to-detector distances were 924 and 1100 mm, respectively (antiscatter grid, focused type; grid ratio, 12:1).

5.2. DE-DT acquisition

Collimator motion was synchronized by measuring the misalignment of the low-voltage (60 kV) and high-voltage (120 kV) images at a constant tube motion. A large energy gap between low and high tube potential kVp imaging yields better material decomposition [28–33]. We selected the abovementioned kV values because this study aimed to improve contrast and artifact reduction during DT acquisition while maintaining an imaging performance similar to that of conventional DT.

Pulsed X-ray exposures and rapid switching between low and high tube potential kVp values were used for DE-DT imaging. Linear system movement and a swing angle of 40° were used when performing tomography, and 37 low- and high-voltage projection images were sampled during a single tomographic pass. We used a low voltage, and each projection image was acquired at 416 mA. A 9.4 ms exposure time was used for low-voltage (60 kV) X-rays at 416 mA, and a 2.5 ms exposure time was used for high-voltage (120 kV) X-rays. To generate reconstructed tomograms of the desired height, we used a 768 × 7684 matrix with 32 bits (single-precision floating number) per image (pixel size, 0.252 mm/pixel; reconstruction interval, 1 mm).

6. Optimization parameter

The experiments were performed according to the scheme shown in **Figure 3**. A range of optional parameters have been identified for IR algorithms. Among these parameters, some are important for determining algorithmic behavior. In this study, we compared the root-mean-square error (RMSE) and mean structural similarity (MSSIM; reconstructed volume image from the previous iterations between the current iteration) to optimize the iteration numbers (i).

The RMSE was defined in this study as follows:

$$RMSE = \sqrt{\frac{\sum_{i=1}^{n}\left(\hat{y}_k - y_k\right)^2}{n}} \tag{18}$$

where y_k is the observed image [current reconstructed image (in-focus plane)], $\hat{y}_k$ is the referenced image [previous reconstructed image (in-focus plane)], and n is the number of compounds in the analyzed set.

The MSSIM of local patterns of luminance- and contrast-normalized pixel intensity were compared to determine the structural similarity (SSIM) index of contrast preservation. This image quality metric is based on the assumed suitability of the human visual system for extracting structure-based information [34].

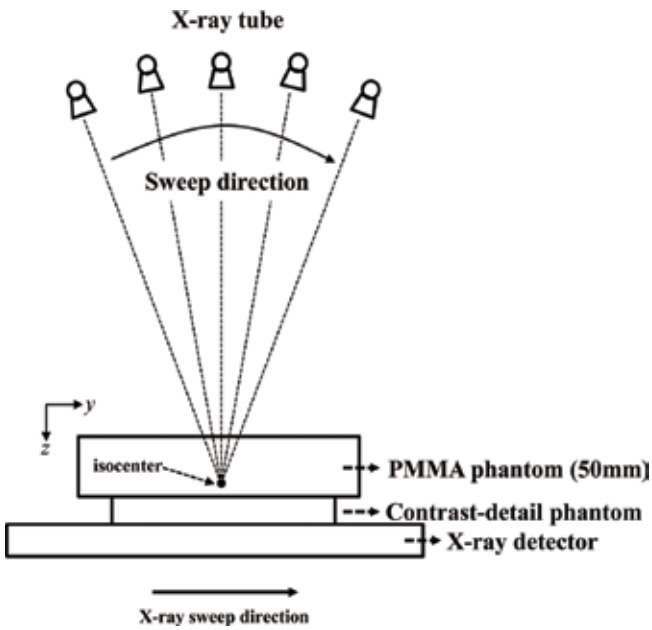

Figure 3. For DT acquisition, the phantom was arranged parallel to the x–y detector plane.

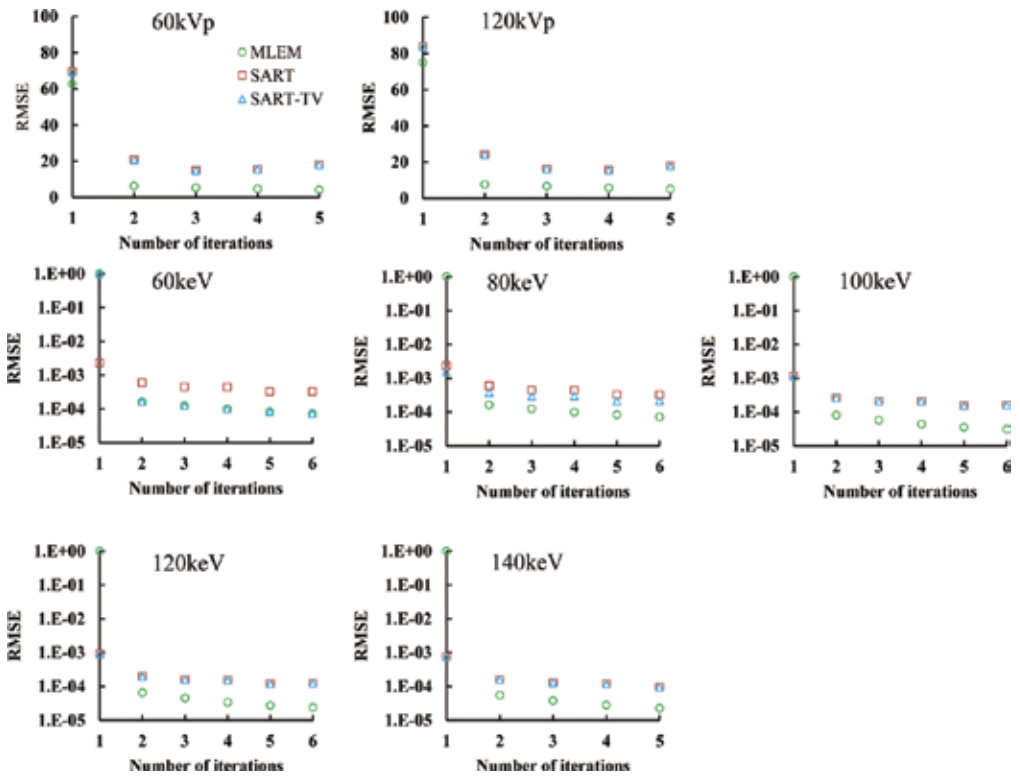

Figure 4. The RMSE characteristics caused by the differences in the number of iterations of each IR algorithm. (60 and 120kVp; polychromatic, 60, 80, 100, 120, and 140 keV; virtual monochromatic).

The SSIM index between pixel values x and y was calculated as follows:

$$SSIM(x,y) = [l(x,y)]^{\alpha} \cdot [c(x,y)]^{\beta} \cdot [s(x,y)]^{\gamma} \tag{19}$$

where l is the luminance, c is the contrast, and s is the structure. Subsequently,

$$\alpha = \beta = \gamma = 1.0$$

The MSSIM was then used to evaluate the overall image quality:

$$MSSIM(X,Y) = \frac{1}{M}\sum_{j=1}^{M} SSIM\left(x_i, y_j\right) \tag{20}$$

where X and Y are the reference [previous reconstructed image (in-focus plane)] and objective [current reconstructed image (in-focus plane)] images, respectively; x_i and y_j are the image contents at the jth pixel; and M is the number of pixels in the image.

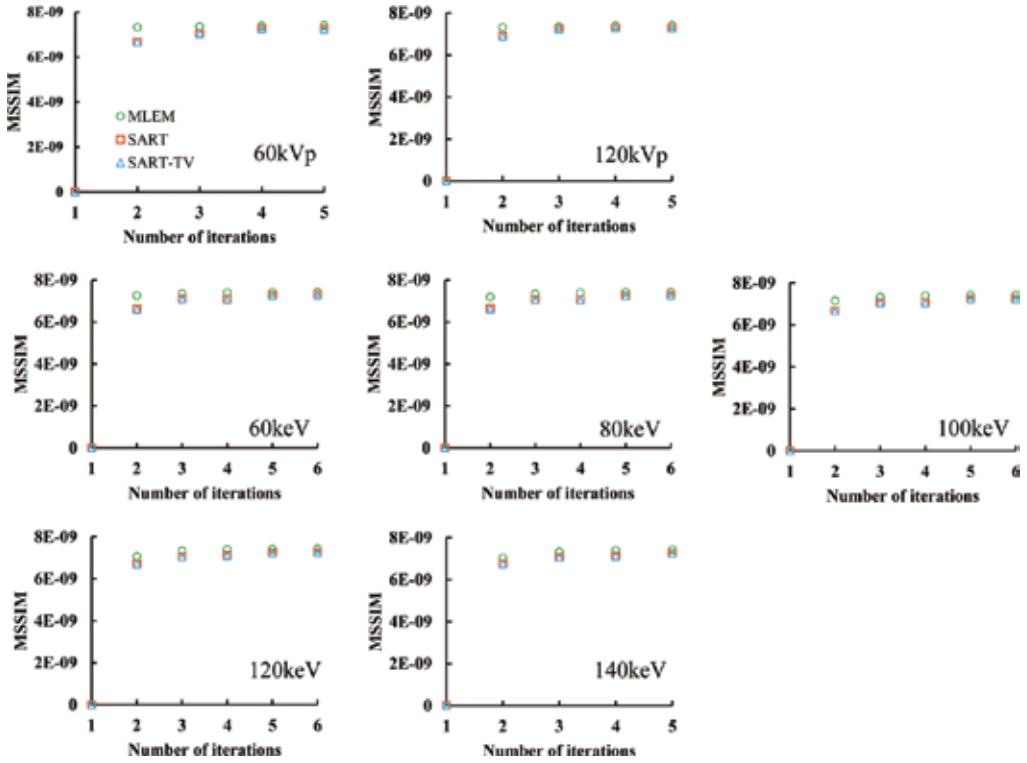

Figure 5. The MSSIM characteristics caused by differences in the number of iterations of each IR algorithm. (60 and 120kVp; polychromatic, 60, 80, 100, 120, and 140 keV; virtual monochromatic).

It was feasible to maintain a steady convergence of polychromatic IR images for inconsistency after the fourth iteration and a convergence of monochromatic IR images for inconsistency after the fifth iteration (**Figures 4** and **5**).

7. Evaluation

The contrast derived from the contrast-to-noise ratio (CNR) in the in-focus plane (15 mm φ; $CaCO_3$, 175 mg/ml, and 100 mg/ml) was also evaluated as a quantitative measure of the reconstructed image quality. In DT, the CNR is frequently used to estimate low-contrast detectability and was defined in this study as follows:

$$CNR = \frac{\mu_{Feature} - \mu_{BG}}{\sigma_{BG}} \tag{21}$$

where $\mu_{Feature}$ is the mean object pixel value, μ_{BG} is the mean background area pixel value, and σ_{BG} is the standard deviation of the background pixel values. The latter parameter includes the

photon statistics, the electronic noise from the results, and the structural noise that could obscure the object. The sizes of all regions of interest (ROIs) used to measure the CNR were adjusted to an internal signal (ROI diameter; eight pixels).

8. Results

Figure 6 shows each density projection image generated by the material decomposition process. A novel DE virtual monochromatic image processing is performed from a density projection image, and **Figures 7** and **8** show the image generated by each reconstruction algorithm.

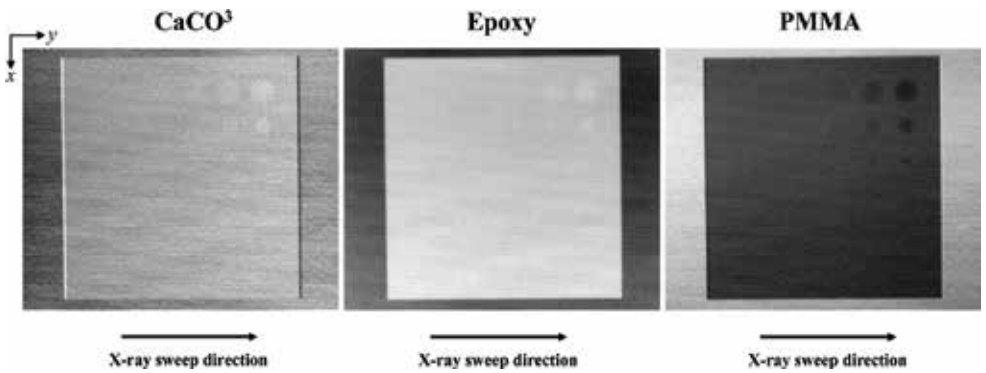

Figure 6. DE material decomposition straight projection images. The DE material decomposition projections for $CaCO_3$, epoxy, and PMMA were window level = 0.59 and window width = 0.26, window level = 0.69 and window width = 0.33, and window level = 0.21 and window width = 0.24, respectively.

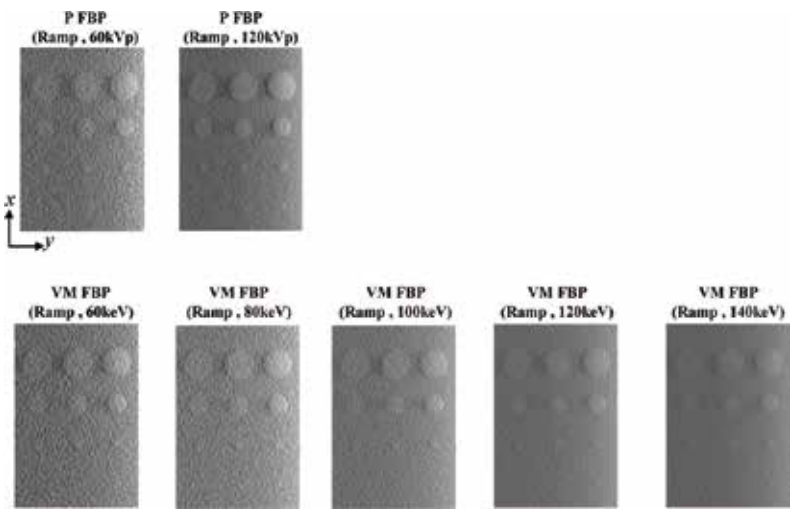

Figure 7. Comparisons among the polychromatic (P) and virtual monochromatic (VM) images acquired by using the FBP reconstruction algorithm (window level = 0.05, window width = 0.11).

http://dx.doi.org/10.5772/intechopen.81667

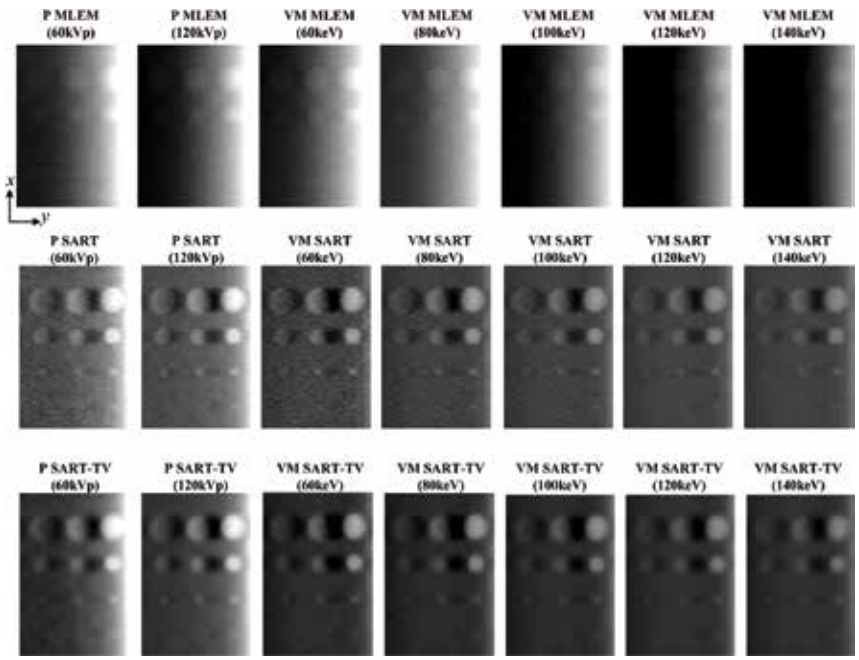

Figure 8. Comparisons among the polychromatic (P) and virtual monochromatic (VM) images with each IR algorithm (P MLEM: Window level = 0.32, window width = 0.17; VM MLEM: Window level = 0.25, window width = 0.12; P&VM SART: Window level = 0.22, window width = 0.37; P&VM SART-TV: Window level = 0.24, window width = 0.34).

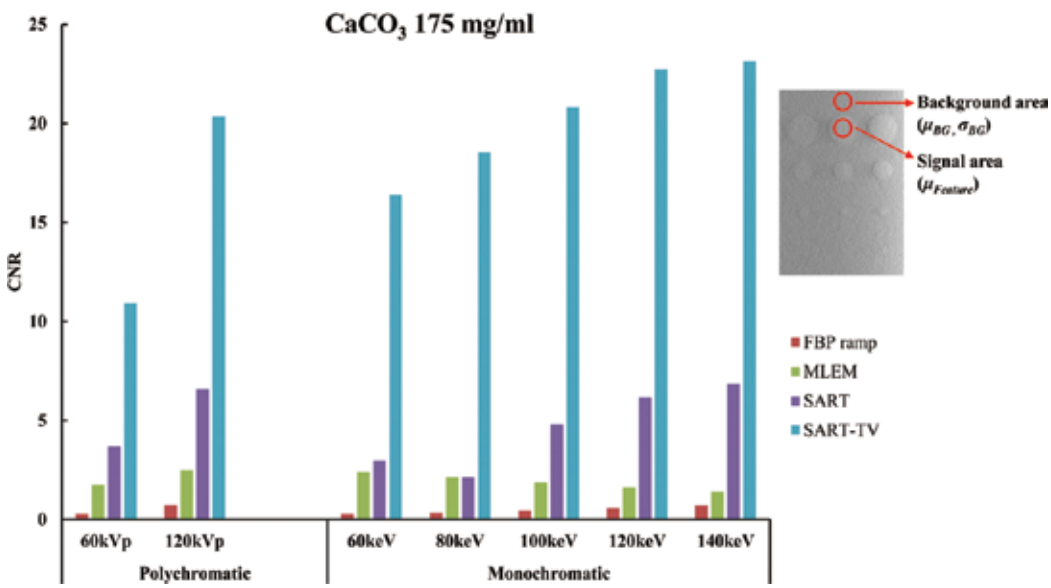

Figure 9. Comparisons of the CNR of the in-focus plane images obtained by using each reconstruction algorithm with polychromatic and virtual monochromatic image processing ($CaCO_3$; 15 mm ϕ, 175 mg/ml).

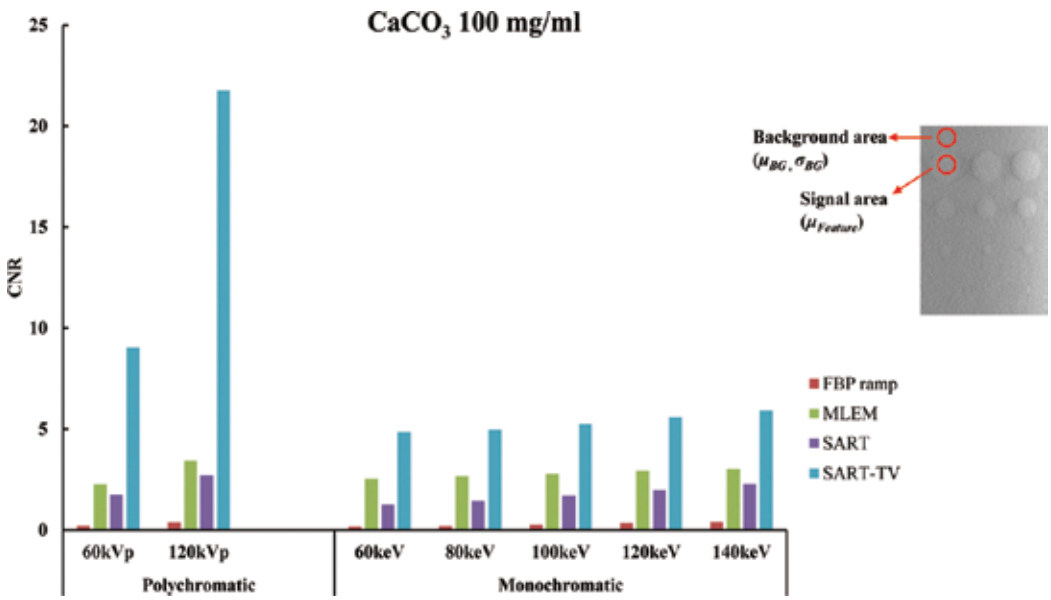

Figure 10. Comparisons of the CNR of in-focus plane images obtained by using each reconstruction algorithm with polychromatic and virtual monochromatic image processing ($CaCO_3$; 15 mm ϕ, 100 mg/ml).

In the novel DE virtual monochromatic image processing performed according to Eq. 17, an image with decreased noise can be obtained as the photon energy was increased. In the conventional polychromatic image, noise is reduced in the high-voltage image. With regard to the contrast extraction capability of high-density objects, the novel DE virtual monochromatic images showed high CNRs. In particular, the SART-TV algorithm provided high-contrast extraction capability (**Figure 9**). Along with the decrease in the concentration of the object, the contrast extraction ability was almost the same for both monochromatic and virtual monochromatic imaging (**Figure 10**).

9. Conclusions

This chapter showed that the novel DE virtual monochromatic image-processing algorithm yielded adequate overall performance. The novel DE virtual monochromatic images produced by using this algorithm yielded good results independent of the type of contrast present in the CD phantom. Furthermore, this processing algorithm successfully removed noise from the images, particularly at high contrast with high-density objects.

In summary, this DE virtual monochromatic image-processing algorithm appears to be a promising new option for DT imaging, as evidenced by the 3D visualizations of high-contrast images that were far superior to those of images processed by conventional single-energy polychromatic image-processing algorithms. The flexibility in the choice of imaging parameters, which is based

on the desired final images and DT imaging conditions, of this novel DE virtual monochromatic image-processing algorithm may be beneficial to users.

Acknowledgements

We wish to thank Mr. Kazuaki Suwa and Yuuki Watanabe at Department of Radiology Dokkyo Medical University Koshigaya Hospital for support on experiment.

Conflict of interest

The authors declare that they have no conflict of interest.

Ethical approval

This article does not contain any studies with human participants or animals performed by any of the authors.

Informed consent

This articles does not contain patient data.

Author details

Tsutomu Gomi

Address all correspondence to: gomi@kitasato-u.ac.jp

Kitasato University, Sagamihara, Japan

References

[1] Ziedses des Plante BG. Eine neue methode zur differenzierung in der roentgenographie (planigraphie). Acta Radiologica. 1932;**13**:182-192

[2] Grant DG. Tomosynthesis. A three-dimensional radiographic imaging technique. IEEE Transactions on Biomedical Engineering. 1972;**19**:20-28

[3] Stiel G, Stiel LG, Klotz E, Nienaber CA. Digital flashing tomosynthesis: A promising technique for angiographic screening. IEEE Transactions on Medical Imaging. 1993;**12**: 314-321

[4] Warp RJ, Godfrey DG, Dobbins JT. Applications of matrix inverse tomosynthesis. Proceedings of SPIE. 2000;**3977**:376-383

[5] Duryea J, Dobbins JT, Lynch JA. Digital tomosynthesis of hand joints for arthritis assessment. Medical Physics. 2003;**30**:325-333

[6] Sone S, Kasuga T, Sakai F, Kawai T, Oguchi K, Hirano H, et al. Image processing in the digital tomosynthesis for pulmonary imaging. European Radiology. 1995;**5**:96-101

[7] Badea C, Kolitsi Z, Pallikarakis N. A 3D imaging system for dental imaging based on digital tomosynthesis and cone beam CT. Proceedings of the International Federation of Medicinal Biology Engineering. 2001;**2**:739-741

[8] Niklason LT, Christian BT, Niklason LE, Kopans DB, Castleberry DE, Opsahl-Ong BH, et al. Digital tomosynthesis in breast imaging. Radiology. 1997;**205**:399-406

[9] Dobbins JT 3rd, Godfrey DJ. Digital x-ray tomosynthesis: Curent state of the art and clinical potential. Physics in Medicine and Biology. 2003;**48**:R65-R106

[10] Kalender WA, Perman WH, Vetter JR, Klotz E. Evaluation of a prototype dual-energy computed tomographic apparatus. I. Phantom studies. Medical Physics. 1996;**13**:334-339

[11] Liu X, Yu L, Primak AN, McCollough CH. Quantitative imaging of element composition and mass fraction using dual-energy CT: Three-material decomposition. Medical Physics. 2009;**36**:1602-1609

[12] Alvarez RE, Macovski A. Energy-selective reconstructions in X-ray computerized tomography. Physics in Medicine and Biology. 1976;**21**:733-744

[13] Kak A, Slaney M. Principles of Computerized Tomographic Imaging. New York: IEEE; 1988

[14] Smith DB. Image reconstruction from cone-beam projections: Necessary and sufficient conditions and reconstruction methods. IEEE Transactions on Medical Imaging. 1985; **M1-4**:14-25

[15] Grangeat P. Mathematical framework of cone-beam 3D reconstruction via the first derivative of the radon transform. Mathematical Methods in Tomography. 1991;**13**:66-97

[16] Feldkamp LA, Davis LC, Kress JW. Practical cone-beam algorithm. Journal of the Optical Society of America. 1984;**A1**:612-619

[17] Ruttimann U, Groenhuis R, Webber R. Restoration of digital multilane tomosynthesis by a constrained iteration method. IEEE Transactions on Medical Imaging. 1984;**MI-3**: 141-148

[18] Bleuet P, Guillemaud R, Magin I, Desbat L. An adapted fan volume sampling scheme for 3D algebraic reconstruction in linear tomosynthesis. IEEE Transactions on Nuclear Science. 2002;**49**:2366-2372

[19] Gordon R, Bender R, Hermen GT. Algebraic reconstruction techniques (ART) for three-dimensional electron microscopy and x-ray photography. Journal of Theoretical Biology. 1970;**29**:471-481

[20] Andersen AH, Kak AC. Simultaneous algebraic reconstruction technique (SART): A superior implementation of the ART algorithm. Ultrasonic Imaging. 1984;**6**:81-94

[21] Du Y, Wang X, Xiang X, Wei Z. Evaluation of hybrid SART + OS + TV iterative reconstruction algorithm for optical-CT gel dosimeter imaging. Physics in Medicine and Biology. 2016;**61**:8425-8439

[22] Candes E, Romberg J, Tao T. Robust uncertainty principles: Exact signal reconstruction from highly incomplete frequency information. IEEE Transactions on Information Theory. 2006;**52**:489-509

[23] Candes E, Romberg J, Tao T. Stable signal recovery from incomplete and inaccurate measurements. Communications on Pure and Applied Mathematics. 2006:1207-1223

[24] Sidky EY, Pan X. Image reconstruction in circular cone-beam computed tomography by constrained, total-variation minimization. Physics in Medicine and Biology. 2008;**53**: 4777-4807

[25] Aharon M, Elad M, Bruckstein A. K-SVD an algorithm for designing overcomplete dictionaries for sparse representation. IEEE Transactions on Signal Processing. 2006;**54**:4311-4322

[26] Leonid IR, Stanley O, Emad F. Nonlinear total variation based noise removal algorithms. Physica D: Nonlinear Phenomena. 1992;**60**:259-268

[27] Berger M, Hubbell J. XCOM: Photon cross sections on a personal computer. National Bureau of Standards Washington, DC (USA) Centre for Radiation Research. 1987:1-28

[28] Pessis E, Campagna R, Sverzut JM, Bach F, Rodallec M, Guerini H, et al. Virtual monochromatic spectral imaging with fast kilovoltage switching: Reduction of metal artifacts at CT. Radiographics. 2013;**33**:573-583

[29] Kuchenbecker S, Faby S, Sawall S, Lell M, Kachelrieß M. Dual energy CT: How well can pseudo-monochromatic imaging reduce metal artifacts? Medical Physics. 2015;**42**:1023-1036

[30] Yue D, Fan Rong C, Ning C, Liang H, Ai Lian L, Ru Xin W, et al. Reduction of metal artifacts from unilateral hip arthroplasty on dual-energy CT with metal artifact reduction software. Acta Radiologica. 2017;**59**:853-860

[31] Yazdi M, Beaulieu L. A novel approach for reducing metal artifacts due to metallic dental implants. IEEE Nuclear Science Symposium Conference Record. 2006;**M06-419**:2260-2263

[32] Hegazy MAA, Eldib ME, Hernandez D, Cho MH, Cho MH, Lee SY. Dual-energy-based metal segmentation for metal artifact reduction in dental computed tomography. Medical Physics. 2018;**45**:714-724

[33] Katsura M, Sato J, Akahane M, Kunimatsu A, Abe O. Current and novel techniques for metal artifact reduction at CT: Practical guide for radiologists. Radiographics. 2018; **38**:450-461

[34] Wang Z, Bovik AC, Sheikh HR, Simoncelli EP. Image quality assessment: From error visibility to structural similarity. IEEE Transactions on Image Processing. 2004;**13**:600-612

Edited by Ronnie A. Sebro

"Medical Imaging and Image-Guided Interventions" is a collection of reviewed and relevant research chapters, offering a comprehensive overview of recent developments in this field of study. This publication aims at providing a thorough overview of the latest research efforts and opens new possible research paths for further novel developments.

Published in London, UK

IntechOpen

ISBN 978-1-83881-190-7